

# The Chamaeleon II low-mass star-forming region: radial velocities, elemental abundances, and accretion properties<sup>\*</sup>

K. Biazzo<sup>1</sup>, J. M. Alcalá<sup>1</sup>, E. Covino<sup>1</sup>, A. Frasca<sup>2</sup>, F. Getman<sup>1</sup>, and L. Spezzi<sup>3</sup>

<sup>1</sup> INAF - Capodimonte Astronomical Observatory, via Moiariello, 16, 80131 Naples, Italy

<sup>2</sup> INAF - Catania Astrophysical Observatory, via S. Sofia, 78, 95123 Catania, Italy

<sup>3</sup> ESO - European Southern Observatory, Karl-Schwarzschild-Str. 2, 85748 Garching bei München, Germany

Received / accepted

## ABSTRACT

**Context.** Knowledge of radial velocities, elemental abundances, and accretion properties of members of star-forming regions is important for our understanding of stellar and planetary formation. While infrared observations reveal the evolutionary status of the disk, optical spectroscopy is fundamental to acquire information on the properties of the central star and on the accretion characteristics.

**Aims.** Existing *2MASS* archive data and the *Spitzer* *c2d* survey of the Chamaeleon II dark cloud have provided disk properties of a large number of young stars. We complement these data with optical spectroscopy with the aim of providing physical stellar parameters and accretion properties.

**Methods.** We use FLAMES/UVES and FLAMES/GIRAFFE spectroscopic observations of 40 members of the Chamaeleon II star-forming region to measure radial velocities through cross-correlation technique, lithium abundances by means of curves of growth, and for a suitable star elemental abundances of Fe, Al, Si, Ca, Ti, and Ni using the code MOOG. From the equivalent widths of the H $\alpha$ , H $\beta$ , and the He I  $\lambda$ 5876,  $\lambda$ 6678,  $\lambda$ 7065 Å emission lines, we estimate the mass accretion rates,  $\dot{M}_{\text{acc}}$ , for all the objects.

**Results.** We derive a radial velocity distribution for the Chamaeleon II stars, which is peaked at  $\langle V_{\text{rad}} \rangle = 11.4 \pm 2.0 \text{ km s}^{-1}$ . We find dependencies of  $\dot{M}_{\text{acc}} \propto M_{\star}^{1.3}$  and of  $\dot{M}_{\text{acc}} \propto \text{Age}^{-0.82}$  in the  $\sim 0.1 - 1.0 M_{\odot}$  mass regime, as well as a mean mass accretion rate for Chamaeleon II of  $\dot{M}_{\text{acc}} \sim 7_{-5}^{+26} \times 10^{-10} M_{\odot} \text{ yr}^{-1}$ . We also establish a relationship between the He I  $\lambda$ 7065 Å line emission and the accretion luminosity.

**Conclusions.** The radial velocity distributions of stars and gas in Chamaeleon II are consistent. The spread in  $\dot{M}_{\text{acc}}$  at a given stellar mass is about one order of magnitude and can not be ascribed entirely to short timescale variability. Analyzing the relation between  $\dot{M}_{\text{acc}}$  and the colors in *Spitzer* *c2d* and *2MASS* bands, we find indications that the inner disk changes from optically thick to optically thin at  $\dot{M}_{\text{acc}} \sim 10^{-10} M_{\odot} \text{ yr}^{-1}$ . Finally, the disk fraction is consistent with the age of Chamaeleon II.

**Key words.** Accretion – Stars: pre-main sequence/low-mass/abundances – Open clusters and associations: individual: Chamaeleon II – Techniques: spectroscopic

## 1. Introduction

The study of accretion properties of members of star-forming regions (SFRs) is important for our understanding of stellar and planetary formation. While infrared observations provide information on the structure of the circumstellar disk, the accretion properties can be retrieved from photometry and spectroscopy using primary diagnostics, such as the UV excess emission (e.g., Gullbring et al. 1998; Rigliaco et al. 2011a), the Paschen/Balmer continuum and Balmer jump (e.g., Gullbring et al. 1998; Herczeg & Hillenbrand 2008; Rigliaco et al. 2011b), or secondary tracers, like hydrogen recombination lines (H $\alpha$ , H $\beta$ , H $\gamma$ , H $\delta$ , Pa $\beta$ , Pa $\gamma$ , Br $\gamma$ ), and the He I, Ca II, Na I lines (e.g., Muzerolle et al. 1998a,b; Natta et al. 2006;

Fang et al. 2009; Rigliaco et al. 2011b; Antonucci et al. 2011). The rate at which the central star accretes from disk material has been found to approximately scale with the square of the stellar mass and to decrease with age (see, e.g., Herczeg & Hillenbrand 2008, and references therein). In addition, the accretion properties are also important to understand the planet-metallicity relation. In fact, the efficiency of dispersal of circumstellar disks is predicted to depend on stellar metallicity in the sense that the formation of planetesimals around stars is faster at higher metallicity (Ercolano & Clarke 2010). Simultaneous measurements of accretion rates and elemental abundances in SFRs and young clusters are therefore crucial to shed light on the role of metallicity in disk dispersal and planetary formation.

The Chamaeleon II (hereafter Cha II) dark cloud, at a distance of  $178 \pm 18 \text{ pc}$  (Whittet et al. 1997), is one of the three main clouds of the Chamaeleon complex ( $\alpha \sim 12^{\text{h}}$ ,  $\delta \sim -78^{\circ}$ ). It extends over  $\sim 2 \text{ deg}^2$  in the sky (see Luhman 2008 for a recent review). The population of Cha II consists of some 20 classical T Tauri stars (CTTSs),  $\sim$ ten weak-

Send offprint requests to: K. Biazzo

<sup>\*</sup> Based on FLAMES (GIRAFFE+UVES) observations collected at the Very Large Telescope (VLT; Paranal, Chile). Program 076.C-0385(A).

Correspondence to: katia.biazzo@oacn.inaf.it

lined T Tauri stars (WTTSs), an intermediate-mass Herbig Ae star (IRAS 12496–7650; see, e.g., Garcia Lopez et al. 2011), a few Herbig-Haro objects (Alcalá et al. 2008, and references therein),  $\sim$ three sub-stellar objects, and references therein) and five very low-mass stars (Spezzi et al. 2008 and references therein). Cha II is one of the five SFRs included in the *Spitzer Space Telescope* Legacy Program “From Molecular Cores to Planet-forming Disks” (*c2d*; Evans et al. 2003; Young et al. 2005; Porras et al. 2007). Through extensive work based on *c2d* IRAC and MIPS *Spitzer* fluxes and complementary data, a reliable census of the population in Cha II (down to  $0.03M_{\odot}$ ) was achieved by Alcalá et al. (2008). They concluded that the cloud is dominated by objects with active accretion, with the Class II sources representing  $\sim 60\%$ . The same sample was investigated spectroscopically in the optical using GIRAFFE/UVES@VLT by Spezzi et al. (2008), who derived stellar parameters and estimated a mean age of  $4 \pm 2$  Myr for Cha II. However, studies of radial velocities, elemental abundances, and accretion properties of the cloud members were not addressed in these works. Recently, Alcalá et al. (2011a) analyzed the star IRAS 12556–7731, concluding that it is indeed a background lithium-rich M-giant star unrelated to Cha II.

As a continuation of the studies by Alcalá et al. (2008) and Spezzi et al. (2008), we derive here radial velocities, elemental abundances, and accretion properties for 40 pre-main sequence (PMS) stars in Cha II. The outline of the paper is as follows. In Sect. 2, we describe the spectroscopic observations and data reduction. In Sect. 3, we report determinations of radial velocities, elemental abundances, and accretion properties. The main results are discussed in Sect. 4, while our conclusions are presented in Sect. 5.

## 2. Spectroscopic observations and data reduction

The observations were conducted in February–March 2006 and February 2007 using FLAMES (GIRAFFE+UVES) at the VLT. A complete journal of the observations and instrumental setup is given in Spezzi et al. (2008). The relevant information for this paper is summarized in Table 1.

We observed 32 objects with GIRAFFE, 11 with UVES, and two with both spectrographs (see Table 1). Despite the  $\sim 25'$  FLAMES field of view (FoV), it was not possible to assign a large number of fibers in each configuration to the PMS objects/candidates because of the large spatial scatter of the targets. The remaining fibers were allocated to young candidates and field stars<sup>1</sup> (numbers in parentheses in columns 4 and 5 of Table 1; see Spezzi et al. 2008 for more details). Thirty-two objects were observed several (2–4) times within two days (see Table 5).

While Spezzi et al. (2008) used a single spectrum per object to derive the spectral type and to confirm the presence of Li I 6708 Å absorption, we use here the complete set of spectra to investigate accretion and short timescale variability. To this aim, we reprocessed the FLAMES/GIRAFFE and FLAMES/UVES observations. The GIRAFFE data were reduced using the GIRAFFE Base-Line Data Reduction Software 1.13.1 (girBLDRS; Blecha et al. 2000): bias and flat subtraction, correction

**Table 1.** Summary of the observations.

Instrument	Range (Å)	Resolution ( $\lambda/\Delta\lambda$ )	# stars	# spectra
GIRAFFE	6438–7164	8 600	32(+27)	69(+45)
UVES	4764–6820	47 000	11	25

for the fiber transmission coefficient, wavelength calibration, and science frame extraction were performed. Then, a sky correction was applied to each stellar spectrum using the task SARITH in the IRAF<sup>2</sup> ECHELLE package and by subtracting the average of several sky spectra obtained simultaneously. The reduction of the UVES spectra was performed using the pipeline developed by Modigliani et al. (2004), which includes the following steps: subtraction of a master bias, échelle order definition, extraction of thorium-argon spectra, normalization of a master flat-field, frame extraction, wavelength calibration, and correction of the science frame for the normalized master flat-field. Sky subtraction was also performed with the IRAF task SARITH using the fibers allocated to the sky.

## 3. Data analysis and results

### 3.1. Radial velocity distribution, membership, and binarity

We determined radial velocities (RVs) of each object, choosing Hn 23 and RX J1303.1–7706 as UVES and GIRAFFE templates, respectively. These slowly rotating stars show no strong accretion signatures (see Table 6). We measured the RV of each template (highest  $S/N$ ) spectrum using the IRAF task RVIDLINES inside the RV package, which considers a line list. We used 50 and 10 lines for the UVES and GIRAFFE spectra, respectively, obtaining  $V_{\text{rad}} = 12.5 \pm 0.4$  km s<sup>−1</sup> for RX J1303.1–7706, and  $V_{\text{rad}} = 15.2 \pm 0.3$  km s<sup>−1</sup> for Hn 23. The heliocentric RV of all targets was determined through the task FXCOR of the IRAF package rv, which cross-correlates the target and template spectra, excluding regions affected by broad lines or prominent telluric features. The centroids of the cross-correlation function (CCF) peaks were determined by adopting Gaussian fits, and the RV errors were computed using a procedure that considers the fitted peak height and the antisymmetric noise (see Tonry & Davis 1979). When more spectra were acquired, we computed the average RV for each object.

In order to estimate the binary fraction, we considered as singles the stars with only one CCF peak and with night-to-night RV variations within  $3\sigma$ . In the end, excluding seven objects for which we could not measure the RV, we find six spectroscopic binaries, which means a binary fraction of 18%. In the last column of Table 5, we list the most probable spectroscopic systems. Five stars are newly identified as spectroscopic binaries, while RXJ1301.0–7654a was already recognized as a double-lined (SB2) spectroscopic system (Covino et al. 1997).

In Fig. 1, we show the Cha II distribution of the RV measurements in the local standard of rest (LSR) obtained

<sup>2</sup> IRAF is distributed by the National Optical Astronomy Observatory, which is operated by the Association of the Universities for Research in Astronomy, inc. (AURA) under cooperative agreement with the National Science Foundation.

<sup>1</sup> Hereafter, we refer to this sample as “field stars”.

from both the UVES and GIRAFFE spectra, along with the RV distribution of the gas derived by Mizuno et al. (1999) from the  $\text{C}^{18}\text{O}$  ( $J = 1 - 0$ ) transition in 11 dense molecular cores in Cha II. Excluding the spectroscopic binaries, the RV distribution of the Cha II members has a mean of  $\langle V_{\text{rad}} \rangle = 11.4 \pm 2.0 \text{ km s}^{-1}$ , which translates to a value of  $\langle V_{\text{LSR}} \rangle = 4.9 \pm 2.0 \text{ km s}^{-1}$ . The Gaussian fit of the distribution yields a mean value peaked at  $\langle V_{\text{LSR}} \rangle = 3.9 \pm 1.6 \text{ km s}^{-1}$ , i.e.  $\langle V_{\text{rad}} \rangle = 10.0 \pm 2.1 \text{ km s}^{-1}$ , which is in fairly good agreement with the average velocity of the gas ( $\langle V_{\text{LSR}} \rangle = 3.0 \pm 0.7 \text{ km s}^{-1}$ , i.e.  $\langle V_{\text{rad}} \rangle = 9.6 \pm 0.7 \text{ km s}^{-1}$  (Mizuno et al. 1999).

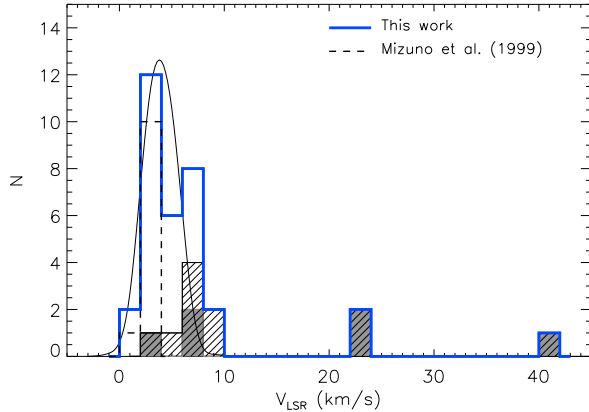


**Fig. 1.** Average RV distribution in the LSR (solid thick line) of the Cha II PMS stars. The distribution of the gas derived by Mizuno et al. (1999) is overlaid (dashed line). The Gaussian fit to the PMS RV distribution is shown (thin line). The shaded histogram represents spectroscopic binary stars, while the hatched one marks the UVES observations. In the case of Hn 24 and Sz 54, where both UVES and GIRAFFE RVs were measured, we considered the UVES observations.

### 3.2. Lithium equivalent width and radial velocity

Lithium equivalent widths ( $EW_{\text{Li}}$ ) were measured by direct integration or by Gaussian fit using the IRAF task SPLOT. Errors in  $EW_{\text{Li}}$  were estimated in the following way: *i*) when only one spectrum was available, the standard deviation of three  $EW_{\text{Li}}$  measurements was adopted; *ii*) when more than one spectrum was gathered, the standard deviation of the measurements on the different spectra was adopted. Typical errors in  $EW_{\text{Li}}$  are of 0.001–0.087 Å (higher values for GIRAFFE data); for the stars C62 and C66,  $\sigma_{EW_{\text{Li}}} \sim 0.15 \text{ Å}$ . Our  $EW_{\text{Li}}$  measurements are consistent with the values of Spezzi et al. (2008) within 0.02 Å.

Figure 2 shows the  $EW_{\text{Li}}$  versus RV for the 37 Cha II members listed in Table 5 (circles) and for the field stars (asterisks). The difference in RV distribution between the no-lithium or weak-lithium stars, and the strong-lithium stars is noticeable. The strong Li stars are confined to a narrow range of velocities (i.e., inside  $\pm 3\sigma$  from the peak of the RV distribution). The strong-lithium sample contains single stars and also the two most probable SB1 systems (C66 and IRAS F13052–7653N) and the two SB2 systems

(RXJ1301.0–7654a and Sz 54), while the rest can be considered as field stars. For the SB2 stars, the average of the RVs of their components falls inside the  $\langle V_{\text{rad}} \rangle \pm 3\sigma$  distribution. The relatively narrow RV distribution of the strong-lithium sample confirms that these stars are all members of the same association.

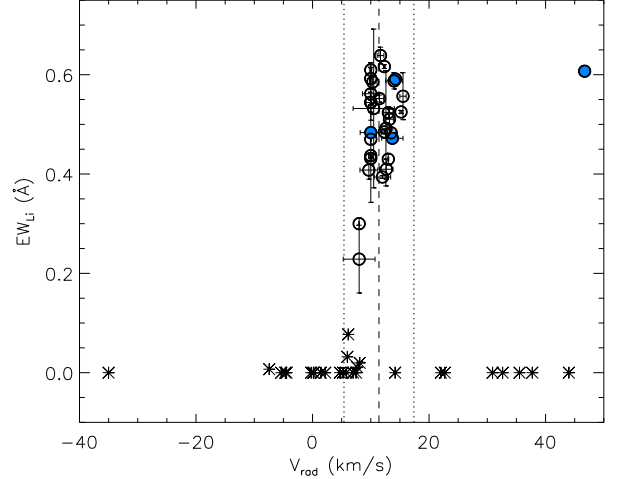


**Fig. 2.**  $EW_{\text{Li}}$  versus RV for stars in the Cha II FoV (see Table 1). Open circles refer to most probable single stars, filled circles are multiple components, and asterisks refer to field stars. We excluded stars whose binarity was detected from RV variation at different phases (namely, Sz51 and Hn 24; see Table 5). In the case of Sz54, observed with both FLAMES configurations, we considered only the UVES RV values. Vertical lines represent the  $\langle V_{\text{rad}} \rangle \pm 3\sigma$  values, where  $\sigma = 2.0 \text{ km s}^{-1}$  (see Section 3.1).

### 3.3. Elemental abundances

#### 3.3.1. Abundance measurements

The FLAMES/UVES wide spectral coverage allows us to select several tens of Fe I+Fe II lines and spectral features of other elements to measure abundances from line EWs. To this aim, as done in Biazzo et al. (2011b), we discarded stars with  $T_{\text{eff}} \lesssim 4000 \text{ K}$  (because of significant formation of molecules in the atmosphere), fast rotators (to avoid rotational blurring), and strong accretors (for which accurate abundance analysis is hampered). In the end, only one star (Hn 23) fulfills the required criteria. Effective temperature and surface gravity ( $\log g$ ) from the literature (Table 7) were used as initial values, and initial microturbulence ( $\xi$ ) was set to  $1.5 \text{ km s}^{-1}$ . Final values of the atmospheric parameters are listed in Table 2, together with abundance determinations, abundance internal errors, and number of lines considered (in parenthesis). The first source of internal error in abundance is due to uncertainties in line EWs, while another contribution comes from the uncertainties in stellar parameters. Systematic (external) errors, introduced by the code and/or model atmosphere, are negligible in comparison with the internal ones (see Biazzo et al. 2011a for details on the treatment of errors).

**Table 2.** Spectroscopic parameters and elemental abundances of Hn 23.

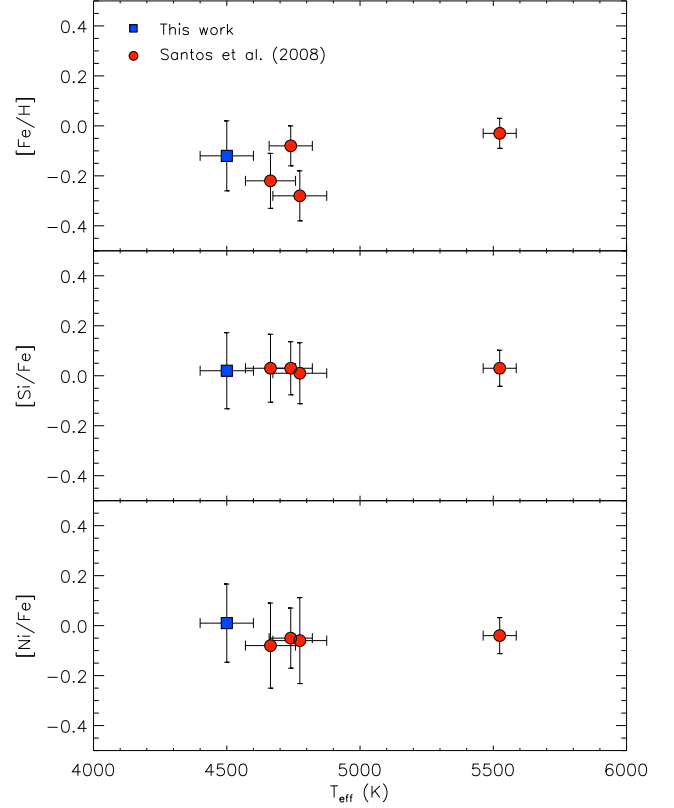
Spectroscopic parameters	
$T_{\text{eff}}$ (K)	$4500 \pm 100$
$\log g$ (dex)	$4.0 \pm 0.2$
$\xi$ (km s $^{-1}$ )	$1.9 \pm 0.2$
Elemental abundances	
[Fe I/H]	$-0.12 \pm 0.14 \pm 0.06(41)$
[Fe II/H]	$-0.13 \pm 0.21 \pm 0.06(3)$
[Al/Fe]	$-0.02 \pm 0.14 \pm 0.05(2)$
[Si/Fe]	$+0.02 \pm 0.15 \pm 0.07(1)$
[Ca/Fe]	$-0.07 \pm 0.15 \pm 0.10(3)$
[Ti I/Fe]	$-0.20 \pm 0.18 \pm 0.09(5)$
[Ti II/Fe]	$+0.04 \pm 0.16 \pm 0.08(1)$
[Ni/Fe]	$+0.01 \pm 0.16 \pm 0.04(7)$

The [Fe/H] value of Hn 23 is slightly below the solar value and in agreement with the mean abundance of  $\langle [\text{Fe}/\text{H}] \rangle = -0.11 \pm 0.11$  found by Santos et al. (2008) for the Chamaeleon Complex (see Fig. 3). This supports the suggestion that SFRs in the solar neighborhood are slightly more metal-poor than nearby young open clusters (Biazzo et al. 2011a). This issue certainly deserves further study, using more stars in the region and homogeneous samples of PMS stars in as many SFRs as possible. Moreover, all other [X/Fe] abundances are close to the solar ones, with silicon and nickel close to the cluster mean value of  $\langle [\text{Si}/\text{Fe}] \rangle = 0.03 \pm 0.01$  and  $\langle [\text{Ni}/\text{Fe}] \rangle = -0.05 \pm 0.02$  found by Santos et al. (2008). Titanium seems to be affected by NLTE effects (see Table 2), as previously found by other authors for stars with temperatures cooler than  $\sim 5000$  K (see, e.g., D’Orazi & Randich 2009; Biazzo et al. 2011a, and references therein). However, detailed treatment of NLTE effects is beyond the scope of this paper.

### 3.3.2. Lithium abundance

Mean lithium abundances were estimated from the average  $EW_{\text{Li}}$  listed in Table 5 and  $T_{\text{eff}}$  values from Spezzi et al. (2008), by using the LTE curves-of-growth reported by Pavlenko & Magazzù (1996) for  $T_{\text{eff}} > 3500$  K, and by Palla et al. (2007) for  $T_{\text{eff}} < 3500$  K. The  $\log g$  values were derived using the effective temperature, luminosity, and mean mass reported for each star in Spezzi et al. (2008). The main source of error in  $\log n(\text{Li})$  comes from the uncertainty in  $T_{\text{eff}}$ , which is  $\Delta T_{\text{eff}} \sim 100$  K (Spezzi et al. 2008). Taking this value and a mean error of  $0.020 \text{ \AA}$  in  $EW_{\text{Li}}$  into account, we estimate a mean  $\log n(\text{Li})$  error ranging from  $\sim 0.07$ – $0.10$  dex for cooler stars ( $T_{\text{eff}} \sim 3200$  K) down to  $\sim 0.05$ – $0.09$  dex for warmer stars ( $T_{\text{eff}} \sim 4200$  K), depending on the  $EW_{\text{Li}}$  value. Moreover, the  $\log g$  value affects the lithium abundance, in the sense that the lower the surface gravity the higher the lithium abundance, and vice versa. In particular, the difference in  $\log n(\text{Li})$  may rise to  $\sim \pm 0.05$  dex when considering stars with mean values of  $EW_{\text{Li}} = 0.500 \text{ \AA}$  and  $T_{\text{eff}} = 4000$  K and assuming  $\Delta \log g = \mp 0.5$  dex.

In Fig. 4 we show the mean lithium abundance as a function of the effective temperature (see Table 5 for the

**Fig. 3.** Iron, silicon, and nickel abundances versus spectroscopic temperature for Hn 23 and the stars analyzed by Santos et al. (2008).

$\log n(\text{Li})$  values). The average of  $\log n(\text{Li})$  is about 2.5 dex with a dispersion of 0.6 dex. The lowest lithium abundance values are presumably due to spectral veiling, which affects the line EW.

### 3.4. Accretion diagnostics and mass accretion rates

The spectral coverage of our data allows us to select several lines (namely, H $\alpha$   $\lambda 6563 \text{ \AA}$ , H $\beta$   $\lambda 4861 \text{ \AA}$ , He I  $\lambda 5876 \text{ \AA}$ , He I  $\lambda 6678 \text{ \AA}$ , and He I  $\lambda 7065 \text{ \AA}$ ) that can be used to determine the accretion luminosity ( $L_{\text{acc}}$ ). These emission lines are powered by processes related to accretion from the circumstellar disk (Herczeg & Hillenbrand 2008). The use of these lines as secondary accretion diagnostics relies on empirical linear relationships between the observed line luminosity ( $L^\lambda$ ) and the accretion luminosity (e.g., Herczeg & Hillenbrand 2008). These relationships have been established through primary diagnostics, such as UV excess emission (Gullbring et al. 1998). We used the  $L^\lambda - L_{\text{acc}}^\lambda$  empirical relations of Herczeg & Hillenbrand (2008) to derive  $L_{\text{acc}}^\lambda$ . The line luminosity was calculated as  $L^\lambda = 4\pi R_\star^2 F^\lambda$ , where the stellar radius,  $R_\star$ , was taken from Spezzi et al. (2008) and the observed flux at the stellar radius,  $F^\lambda$ , was derived by multiplying the EW of each line ( $EW_\lambda$ ) by the continuum flux at wavelengths adjacent to the line ( $F_{\text{continuum}}^{\lambda \pm \Delta\lambda}$ ). The latter was gathered from the NextGen Model Atmospheres (Hauschildt et al. 1999), assuming the corresponding stellar temperature and gravity (see Table 7). The mass accretion rate,  $\dot{M}_{\text{acc}}^\lambda$ , was then de-

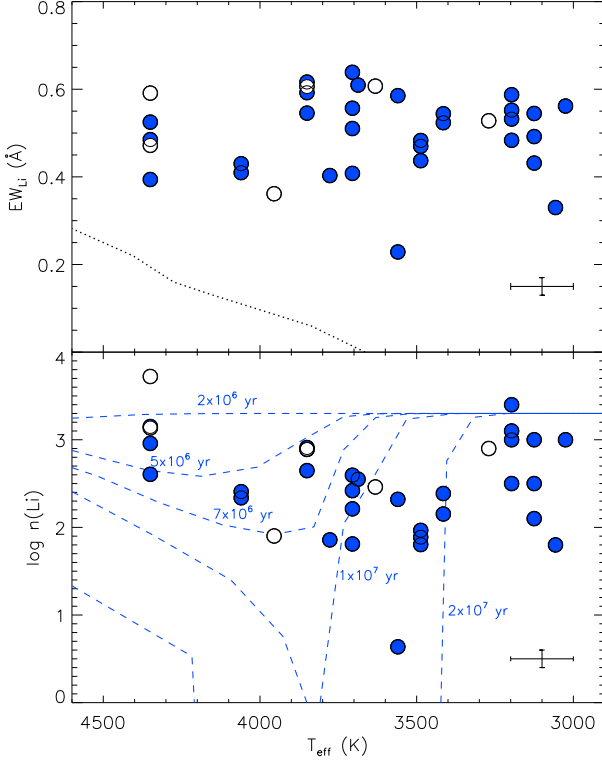


**Fig. 4.** *Upper panel:*  $EW_{\text{Li}}$  versus effective temperature. The upper envelope for the Pleiades, as adapted by Soderblom et al. (1993), is overplotted as a dotted line. *Lower panel:* Lithium abundance versus effective temperature. The “lithium isochrones” by D’Antona & Mazzitelli (1997) in the 2–20 Myr range are overlaid with dashed lines. In both panels, empty symbols represent spectroscopic binaries, while mean error bars are overplotted on the lower right corner.

rived from  $L_{\text{acc}}^{\lambda}$  using the following relationship (Hartmann 1998):

$$\dot{M}_{\text{acc}}^{\lambda} = \left(1 - \frac{R_{\star}}{R_{\text{in}}}\right)^{-1} \frac{L_{\text{acc}}^{\lambda} R_{\star}}{GM_{\star}}, \quad (1)$$

where the stellar radius  $R_{\star}$  and mass  $M_{\star}$  for each star were taken from Spezzi et al. (2008), and the inner-disk radius  $R_{\text{in}}$ , when available, from Alcalá et al. (2008). When no  $R_{\text{in}}$  was available, we assumed  $R_{\text{in}} = 5R_{\star}$  (see Hartmann 1998), which is a good approximation for most accretors, as pointed out by Alcalá et al. (2011b). Contributions to the error budget on  $\dot{M}_{\text{acc}}$  include uncertainties on stellar mass, stellar radius, inner-disk radius, and  $L_{\text{acc}}^{\lambda}$ . Assuming mean errors of  $\sim 0.15M_{\odot}$  in  $M_{\star}$  (Spezzi et al. 2008),  $\sim 0.10R_{\odot}$  in  $R_{\star}$  (Spezzi et al. 2008), and  $\sim 0.2$  AU in  $R_{\text{in}}$  (Alcalá et al. 2008), 5–10% as relative error in  $EW_{\lambda}$ , 10% in  $F_{\text{continuum}}^{\lambda \pm \Delta\lambda}$ , and the uncertainties in the relationships by Herczeg & Hillenbrand (2008), we estimate a typical error in  $\log \dot{M}_{\text{acc}}$  of  $\sim 0.5$  dex.

Apart from variability phenomena, which will be discussed in Section 4.2, the mass accretion rates derived from the various diagnostics should be consistent with each other. In the following, we describe the results drawn from the hydrogen and helium emission lines.

Figure 5 (upper panel) shows the mean accretion luminosity<sup>3</sup>, derived from the  $H\alpha$  emission line, versus the mean accretion luminosities obtained from other hydrogen and helium emission lines. A fairly good agreement between these diagnostics is present. Comparing the mean mass accretion rate from the  $H\alpha$  line with the mean  $\dot{M}_{\text{acc}}$  as obtained through the other diagnostics, the agreement is well reproduced (see lower panel in Fig. 5 and column 16 in Table 6). This justifies the use of all the diagnostics to compute an average  $\langle L_{\text{acc}} \rangle$ <sup>4</sup> (and, hence, also an average  $\langle \dot{M}_{\text{acc}} \rangle$ ) for each star. A weighted average of  $\langle L_{\text{acc}} \rangle$  derived from the  $H\alpha$ ,  $H\beta$ ,  $\text{He I } \lambda 5876 \text{ \AA}$ , and  $\text{He I } \lambda 6678 \text{ \AA}$  emission lines allows us to analyze the relationship between  $\langle L_{\text{acc}} \rangle$  and the luminosity in the  $\text{He I } \lambda 7065 \text{ \AA}$  line, which is shown in Fig. 6. A linear fit to the relationship gives

$$\langle \log L_{\text{acc}}^{\text{He } \lambda 7065} \rangle = (4.01 \pm 0.35) + (1.14 \pm 0.06) \langle \log L^{\text{He } \lambda 7065} \rangle. \quad (2)$$

The good correlation justifies the use of the  $\text{He I } \lambda 7065 \text{ \AA}$  line as the reliable diagnostic of  $L_{\text{acc}}$ .

As already pointed out, the different line diagnostics yield consistent mass accretion rates (see Fig. 5 and Table 6). Considering, for instance, the  $H\alpha$  line, which is observed in all targets, the mean difference in  $\log \dot{M}_{\text{acc}}^{\text{H}\alpha}$  as compared to  $\log \dot{M}_{\text{acc}}^{\text{H}\beta}$  is of  $0.3 \pm 0.3 M_{\odot} \text{ yr}^{-1}$  (with a maximum of 0.8 dex observed for Sz 54), while it is  $-0.2 \pm 0.4$  dex with respect to  $\log \dot{M}_{\text{acc}}^{\text{He } \lambda 5876}$  (with a maximum of  $-0.2$  dex observed for Sz 56), and  $0.1 \pm 0.5$  dex with respect to  $\log \dot{M}_{\text{acc}}^{\text{He } \lambda 6678}$  (with a maximum of 1.1 dex for Sz 50). The mass accretion rate for the sample is in the range  $10^{-11} \div 2 \times 10^{-8} M_{\odot} \text{ yr}^{-1}$ , which is typical of Class II low-mass YSOs (see Fig. 2 in Sicilia-Aguilar et al. 2010). Excluding multiple systems, stars with  $EW_{\text{H}\alpha} \leq 10 \text{ \AA}$ , and the early-type star DK Cha, we find an average mass accretion rate for Cha II of  $\langle \dot{M}_{\text{acc}} \rangle \sim 7 \times 10^{-10} M_{\odot} \text{ yr}^{-1}$ .

### 3.4.1. Comparison with previous studies

Fourteen of our targets were also analyzed by Antonucci et al. (2011) as part of the POISSON (Protostellar Objects IR-optical Spectral Survey On NTT) project aimed at deriving the mass accretion rates of young stars in star-forming regions through low-resolution optical/near-IR spectroscopy. Antonucci et al. (2011) used the  $\text{Br}\gamma$  line as an accretion tracer. They argue that this is the best diagnostic in their spectra when compared with other tracers (i.e.,  $\text{Pa}\gamma$ ,  $\text{Ca II}$ ,  $\text{H}\alpha$ , and  $[\text{O I}]$ ). Comparing their  $\log \dot{M}_{\text{acc}}$  with our mean  $\log \dot{M}_{\text{acc}}$ , their values tend to be systematically higher than ours. In particular, their values strongly diverge from ours at  $\log \dot{M}_{\text{acc}} < -8$ , with a mean difference of  $1.0 \pm 0.8$  dex. An analogous trend was found by the same authors when comparing  $L_{\text{acc}}^{\text{Pa}\beta, [\text{O I}], \text{H}\alpha, \text{Ca II}}$  with  $L_{\text{acc}}^{\text{Br}\gamma}$  (see their Fig. 4), which is more evident in their  $L_{\text{acc}}^{\text{H}\alpha} - L_{\text{acc}}^{\text{Br}\gamma}$  diagram. They ascribe this behavior to enhanced chromospheric emission or absorption from outflowing material, direct photoionization at higher luminosities, or flux losses due to winds.

When comparing the POISSON’s  $EW_{\text{H}\alpha}$  with the values derived by us (left-hand panel of Fig. 7), the difference

<sup>3</sup> This is the average of different observations for a given star.

<sup>4</sup> This is the average of different diagnostics.



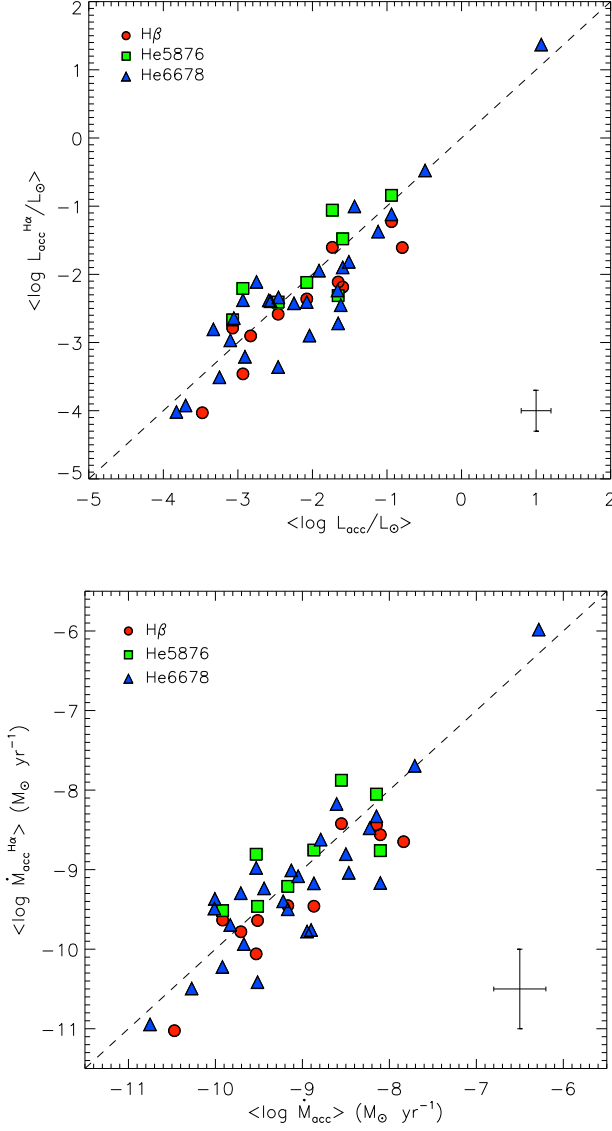


**Fig. 5.** Average  $L_{\text{acc}}^{\text{H}\alpha}$  (top panel) and  $\dot{M}_{\text{acc}}^{\text{H}\alpha}$  (bottom panel) derived from the  $\text{H}\alpha$  line as a function of  $\langle L_{\text{acc}}^{\lambda} \rangle$  and  $\langle \dot{M}_{\text{acc}}^{\lambda} \rangle$  obtained from the  $\text{H}\beta$ ,  $\text{He I } \lambda 5876 \text{ \AA}$ , and  $\text{He I } \lambda 6678 \text{ \AA}$  lines. Mean error bars are overplotted on the lower right corner of each panel.

is  $\Delta EW_{\text{H}\alpha} = 10 \pm 23 \text{ \AA}$ . Considering that the observations were performed at different epochs (our run was in 2006, while their run was in 2009) and that their  $EW_{\text{H}\alpha}$  were measured on low-resolution spectra ( $R \sim 700$ ), the agreement is fairly good. In fact, a good correlation is found between our estimated  $\text{H}\alpha$  line luminosities and the POISSON's values, with a difference of  $0.04 \pm 0.13 L_{\odot}$  (see Fig. 7, middle panel). Thus, the differences in mass accretion rate arise when deriving  $L_{\text{acc}}$ . A similar behavior as the one shown in Fig. 7 for the mass accretion rate is found when our  $L_{\text{acc}}$  values are compared with those of POISSON, in agreement with the results by Antonucci et al. (2011). This means that the differences between POISSON and our determinations are mainly due to the tracers used to derive  $L_{\text{acc}}$ . As shown in Fig. 5, very good correlations of  $L_{\text{acc}}$

as derived from the  $\text{He I}$  and  $\text{H}\alpha$  lines are found. Should there be an important contribution to the line diagnostics by winds and/or chromospheric activity, our estimates of  $L_{\text{acc}}$  would be in excess with respect to those derived from the  $\text{Br}\gamma$  line. Instead, the opposite is observed. We thus exclude the possibility that the differences are due to the influence of winds and chromospheric activity. A possible explanation for the difference between our average  $L_{\text{acc}}$  values and the POISSON's  $L_{\text{acc}}^{\text{Br}\gamma}$  may be that the various accretion diagnostics originate in different regions at different physical conditions. In order to investigate this issue, measurements of primary accretion tracers, and  $\text{Br}\gamma$  measurements are needed. Such analysis cannot be conducted with the data available here, but will be addressed in our future studies exploiting X-Shooter@VLT data (cf. Alcalá et al. 2011b).

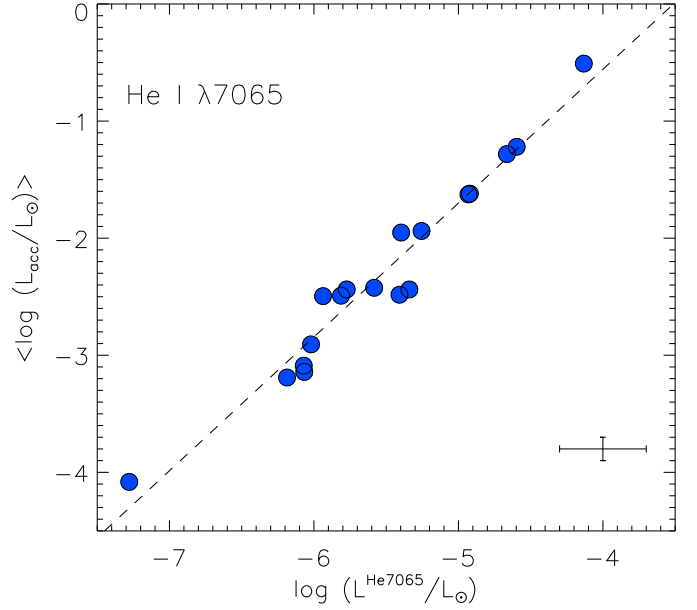


**Fig. 6.** Average accretion luminosity versus line luminosity for the  $\text{He I } \lambda 7065 \text{ \AA}$  line. The linear fit given in the text (Equation 2) is represented by the dashed line. Mean error bars are overplotted on the lower right corner.

### 3.4.2. Other lines in the optical

A number of optical lines are seen in emission in the spectra of several stars in our sample. These are the forbidden lines of  $[\text{O I}] \lambda 6300.3 \text{ \AA}$ , and  $\lambda 6363.8 \text{ \AA}$ ,  $[\text{S II}] \lambda 6715.8 \text{ \AA}$ , and  $\lambda 6729.8 \text{ \AA}$ ,  $[\text{N II}] \lambda 6548.4 \text{ \AA}$ , and  $\lambda 6583.4 \text{ \AA}$ , as well as  $\text{Fe II}$  multiplets. These lines trace mainly stellar/disk winds, jets, disk surfaces, and outflow activity (Cabrit et al. 1990; Hartigan et al. 1995), and their detailed treatment is beyond the scope of this paper. Here, we only note that the  $[\text{O I}] \lambda 6300.3 \text{ \AA}$  line is detected in 6/11 objects, the  $[\text{O I}] \lambda 6363.8 \text{ \AA}$  line in 1/11 objects, the  $[\text{S II}] 6715.8 \text{ \AA}$  and  $6729.8 \text{ \AA}$  emission is observed in 7/40 and 9/40 sources, respectively, and the  $[\text{N II}] 6548.4 \text{ \AA}$  and  $6583.4 \text{ \AA}$  lines are present in 5/40 and 5/40 stars (see Table 5). In the case of Sz 51, the star showing the strongest  $\text{H}\alpha$  in our FLAMES/UVES sample, there is evidence of other emission lines (such as the  $\text{Mg I}$  triplet at  $\lambda 5167.3$ ,  $5172.7$ ,

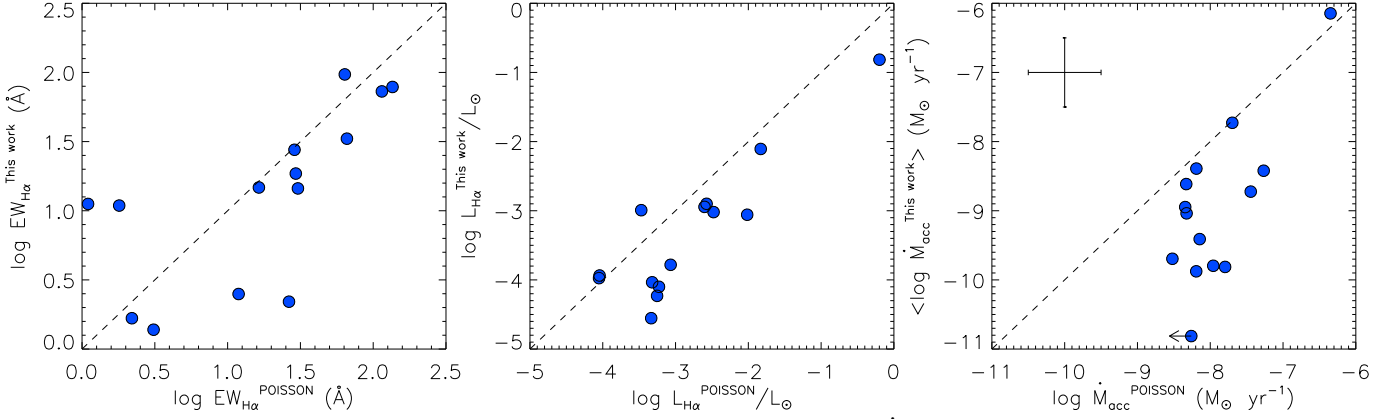


**Fig. 7.** Comparison between our  $EW_{H\alpha}$  (left panel),  $L_{H\alpha}$  (middle panel), and  $\dot{M}_{acc}$  (right panel) values and those obtained by Antonucci et al. (2011). In the right panel, mean error bars are overplotted on the upper left corner.

5183.6 Å, the multiplets 42 and 49 of Fe II, etc.) indicating mass loss.

## 4. Discussion

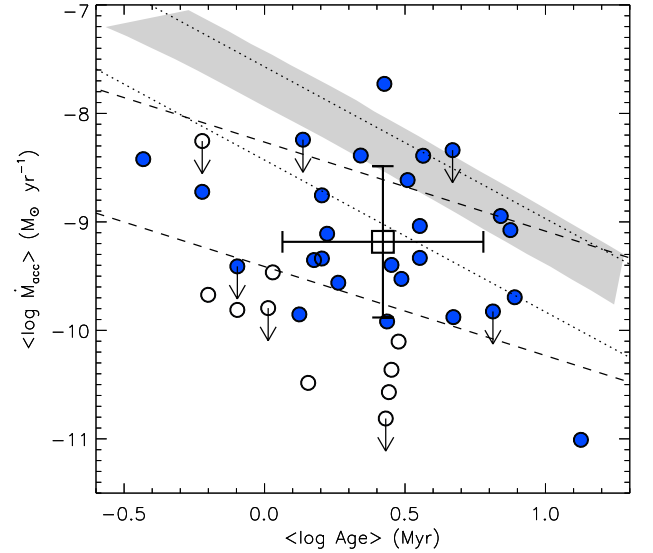
### 4.1. Accretion versus stellar age and mass

Figure 8 shows the mean mass accretion rate versus stellar age (see Table 7) for all the targets except the early-type star DK Cha, which has a massive disk and high  $\dot{M}_{acc}$  (Sicilia-Aguilar et al. 2010). A slightly decreasing trend with age may be present, though over a narrow age interval ( $\sim 0.4 - 13.4$  Myr) and with a large scatter in  $\dot{M}_{acc}$ . This would be consistent with the evolution of a viscous disk (see, e.g., Hartmann et al. 1998; Sicilia-Aguilar et al. 2010, and references therein), although the mean  $\dot{M}_{acc}$  is slightly lower than that expected from the model at the Cha II age. In order to quantify the degree of anti-correlation between  $\log \dot{M}_{acc}$  and  $\log Age$ , we calculated the Spearman's rank correlation coefficient using the IDL procedure R\_CORRELATE (Press et al. 1996). We find a correlation coefficient  $\rho = -0.38$ , with a probability of obtaining such  $\rho$  from randomly distributed data of  $p = 0.08$ . This seems to confirm a moderate anti-correlation between  $\dot{M}_{acc}$  and age, with an average mass accretion rate of  $7^{+26}_{-5} \times 10^{-10} M_{\odot} \text{ yr}^{-1}$  at a mean age of  $3^{+3}_{-1}$  Myr. The linear relation we obtain for the likely single stars with mean  $EW_{H\alpha}$  higher than 10 Å is

$$\langle \log \dot{M}_{acc} (M_{\odot} \text{ yr}^{-1}) \rangle = -8.84 \pm 0.22 - 0.82 \pm 0.40 \log Age \text{ (Myr)} \quad (3)$$

The slope is higher than, yet consistent within the errors with, that obtained by Hartmann et al. (1998) in Cha I (i.e.,  $\log \dot{M}_{acc} (M_{\odot} \text{ yr}^{-1}) = -8.00 \pm 0.10 - 1.40 \pm 0.29 \log Age \text{ (Myr)}$ ). We warn, however, about the large uncertainties in absolute ages derived from theoretical models for stars younger than  $\sim 10$  Myr (see, e.g., Spezzi et al. 2008). We note also that a strong constraint on the apparent trend in  $\log \dot{M}_{acc}$  versus age is set by only one object in the sample (C41, age  $\sim 13$  Myr). The trend disappears if this object is not considered.

Figure 9 shows the mean mass accretion rate versus mean stellar mass (see Table 7). Taking into account sin-



**Fig. 8.** Mean mass accretion rate versus age. Open symbols represent the targets with mean  $EW_{H\alpha} \leq 10$  Å, while binaries are evidenced as upper limits. The big square represents the mean position of Cha II, taking into account the single stars with mean  $EW_{H\alpha} > 10$  Å (vertical and horizontal error bars correspond to the standard deviations from the mean  $\dot{M}_{acc}$  and age, respectively). The dashed lines mark minimum and maximum limits of Eq. 3, while dotted lines represent the analogous limits of the relationship derived for Cha I by Hartmann et al. (1998). The collection of viscous disk evolutionary models for solar-type stars with initial disk masses of  $0.1 - 0.2 M_{\odot}$ , constant viscosity  $\alpha = 10^{-2}$ , and viscosity exponent  $\gamma = 1$  reported by Sicilia-Aguilar et al. (2010) is also displayed (filled region).

gle stars with  $EW_{H\alpha} > 10$  Å, we find the following linear relationship:

$$\langle \log \dot{M}_{acc} (M_{\odot} \text{ yr}^{-1}) \rangle = -8.64 \pm 0.21 + 1.30 \pm 0.41 \log M_{\star} (M_{\odot}), \quad (4)$$

where the slope is slightly lower than that found for Cha I ( $\sim 2$ ; see Antonucci et al. 2011, and references therein). A

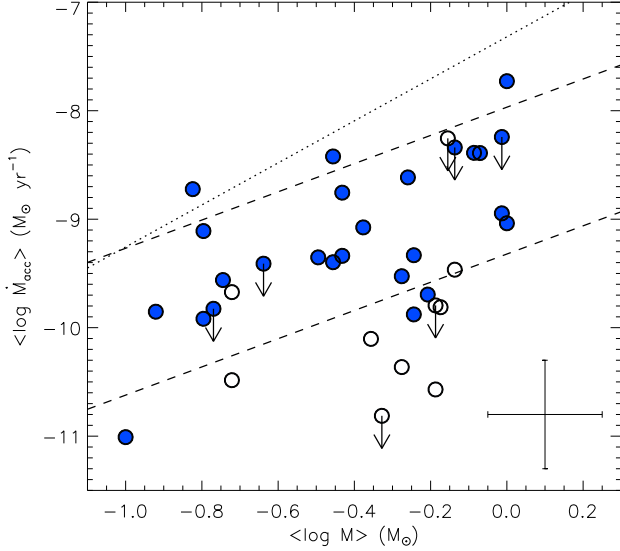


**Fig. 9.** Mean mass accretion rate versus mean stellar mass. Symbols as in Fig. 8. The dashed lines mark minimum and maximum limits of Eq. 4, while the dotted line represents the mean relationship derived for Cha I by Antoniucci et al. (2011). Mean error bars are overplotted on the lower right corner.

correlation of  $\dot{M}_{\text{acc}}$  with stellar mass is evident. Spearman's rank correlation coefficient is  $\rho = 0.51$  with a probability  $p = 0.02$ . The exponent of the  $\dot{M}_{\text{acc}} - M_{\star}$  power law is consistent with the range of values  $\sim 1.0 - 2.8$  found for low-mass stars in other SFRs (see, e.g., Herczeg & Hillenbrand 2008, Fang et al. 2009; Antoniucci et al. 2011, and references therein).

#### 4.2. Short timescale variability

Young PMS stars are known to be variable, due to the combination of different processes (Herbst et al. 1994) occurring on different timescales: on short timescale (days), variability can be induced by rotation of cool or hot spots (type I variability), and on long timescales (months–years), accretion rate changes (type II variability) or obscuration by circumstellar dust might occur (type III variability, e.g., Schisano et al. 2009). The time span of our observations is  $\sim 48$  hours. Emission line variability on timescales shorter than two days is observed for several objects and for all the analyzed lines (see Fig. B.1). In particular, Figs. A.1, A.2, and A.3 show the  $H\alpha$  and  $H\beta$  profiles of the stars displaying the strongest line variations, while Fig. B.1 shows the mass accretion rates derived from the  $H\alpha$ ,  $H\beta$ ,  $\text{He I } \lambda 5876 \text{ \AA}$ , and  $\text{He I } \lambda 6678 \text{ \AA}$  lines versus stellar mass. The vertical bars in these plots represent the range of  $\dot{M}_{\text{acc}}$  as due to the two-day variability of the corresponding diagnostics.

In general, on the timescale of only two days, the  $H\alpha$  equivalent width of some stars changes up to a factor of 2–3 and, *assuming* that this is due to accretion, variation in  $\log \dot{M}_{\text{acc}}$  would be 0.2–0.6 dex, i.e., a factor of 1.6–4.0. We conclude that this  $\log \dot{M}_{\text{acc}}$  variability, even if large, cannot explain the  $\log \dot{M}_{\text{acc}}$  spread at a given mass. This

means that other stellar properties besides mass must also affect the variations.

#### 4.3. Accretion and Metallicity

Investigating the dependency of the mass accretion rate upon iron abundance in SFRs is important for two reasons. First, while the correlation between stellar metallicity and presence of giant planets around solar-type stars is well established (see, e.g., Johnson et al. 2010 and references therein), the metallicity-planet connection in the early stages of planetary formation is still a matter of debate. The evolution of  $\dot{M}_{\text{acc}}$  is affected by possible planetary formation in the disk, and hence it might provide important clues on the planet-metallicity correlation. Second, the efficiency of the dispersal of circumstellar (or protoplanetary) disks and hence the dispersal timescale are predicted to depend on metallicity in the sense that planetary formation is faster in disks with higher metallicity (Ercolano & Clarke 2010). Yasui et al. (2010) find that the disk fraction in significantly low-metallicity clusters ( $[\text{O}/\text{H}] \sim -0.7$ ) declines rapidly in  $< 1$  Myr, which is much faster than the value of  $\sim 5 - 7$  Myr observed in solar-metallicity clusters. Since the shorter disk lifetime reduces the time available for planetary formation, they suggest that this could be one of the reasons for the strong planet-metallicity correlation.

Recent studies by De Marchi et al. (2011) and Spezzi et al. (2012) in the Large and Small Magellanic Clouds show that metal-poor stars accrete at higher rates compared with solar-metallicity stars in galactic SFRs. Summarizing the mean  $\dot{M}_{\text{acc}}$  of low-mass ( $0.1 - 1.0 M_{\odot}$ ) Class II stars members of  $\sim 3 - 4$  Myr old nearby SFRs for which iron abundance has been recently measured (see Table 3), it is only possible to point out that for  $[\text{Fe}/\text{H}] \sim 0$  the mass accretion rate is  $\sim 10^{-10} M_{\odot} \text{ yr}^{-1}$ .

#### 4.4. Fraction of accretors versus age

Excluding the six spectroscopic binaries, 27 of the studied stars result in having mean  $EW_{H\alpha}$  higher than  $10 \text{ \AA}$ , which would imply a percentage of accretors of about  $26/34 = 79\%$  (34 being the total number of single stars in the sample). However, the majority of PMS stars in Cha II have a spectral type later than K7, with most of them later than M3. Therefore, according to the criterion by White & Basri (2003), a more adequate dividing line between most probable accretors and non-accretors in Cha II is  $EW_{H\alpha} = 20 \text{ \AA}$ . Using this criterion, 19 stars can be classified as true accretors, leading to a percentage of  $\sim 55 \pm 5\%$ . This fraction of accretors is consistent with the average age of the cloud members. In fact, following the mass accretion rate evolution with time shown in Fig. 3 of Fedele et al. (2010), the fraction of stars with ongoing mass accretion decreases fast with age, going from  $\sim 60\%$  at  $1.5 - 2.0$  Myr down to  $\sim 2\%$  at  $10$  Myr.

#### 4.5. Color- $\dot{M}_{\text{acc}}$ diagrams

Near-infrared colors can be used to probe the inner disk region. Hartigan et al. (1995), studying a sample of 42 T Tauri stars and using the  $K - L$  color excesses, pointed out that the disk dispersion is mainly due to the formation of micron-sized dust particles, which combine to



**Table 3.** Iron abundances and mass accretion rates in nearby SFRs.

Star-Forming Region	[Fe/H] (dex)	Reference	$\dot{M}_{\text{acc}}$ ( $M_{\odot} \text{ yr}^{-1}$ )	Reference
Orion Nebula Cluster	$-0.13 \pm 0.02$	Biazzo et al. (2011a)	$3 \times 10^{-9}$	Robberto et al. (2004)
$\sigma$ Orionis	$-0.02 \pm 0.09$	González-Hernández et al. (2008)	$3 \times 10^{-10}$	Rigliaco et al. (2011a)
Taurus	$0.00 \pm 0.07$	D’Orazi et al. (2011)	$3 \times 10^{-9}$	Güdel et al. (2007)
Chamaeleon II	$-0.12 \pm 0.14$	This work	$7 \times 10^{-10}$	This work

create planetesimals and protoplanets at the end of the CTTS phase. Protoplanets may clear the inner disk of gas and dust, causing the disk to lose its near-infrared color excess and at the same time opening a gap in the disk (Lin & Papaloizou 1993), thereby terminating accretion from the disk onto the star.

With the aim of investigating possible relationships between near-infrared colors and accretion properties, we used *2MASS* and *Spitzer*<sup>5</sup> colors (see Figs. 10 and 11). We considered these colors as disk tracers from the inner to the outer zone because they may estimate the magnitude of the near- and mid- infrared excesses above the photospheric level. In order to quantify the degree of correlation between these diagnostics, we calculated the Spearman’s rank correlation coefficient, as we did in Section 4.1, and considered Class II stars with  $EW_{\text{H}\alpha} > 10 \text{ \AA}$ . The correlation coefficients, together with the probabilities, are listed in Table 4 and show that the best agreements are obtained for the  $Ks-[8.0]$  and  $[3.6]-[4.5]$  colors versus  $\langle \log \dot{M}_{\text{acc}} \rangle$  parameters. Also,  $Ks-[4.5]$ ,  $Ks-[5.8]$ ,  $[3.6]-[5.8]$ , and  $[3.6]-[8.0]$  colors versus  $\langle \log \dot{M}_{\text{acc}} \rangle$  show good agreement. This implies that objects with detectable accretion have optically thick inner disks. In particular, we can define the regions where  $\dot{M}_{\text{acc}} > 1.0 \times 10^{-10} M_{\odot} \text{ yr}^{-1}$  and  $Ks-[8.0] > 1.5$  or  $[3.6]-[4.5] > 0.2$ , or  $[3.6]-[5.8] > 0.5$ , or  $[3.6]-[8.0] > 0.9$  as those where accreting objects with infrared excess are found in Cha II. The value  $\dot{M}_{\text{acc}} \sim 10^{-10} M_{\odot} \text{ yr}^{-1}$  is a reasonable threshold for the transition from optically thick to optically thin (inner) disk (D’Alessio et al. 2006), as also found by Rigliaco et al. (2011a) in the  $\sigma$  Orionis SFR. The rough trend we tentatively observe among optically thin and optically thick disks, which needs to be confirmed on larger samples, might indicate a link between the mass accretion rate and the grain properties. This link, in turn controls the disk geometry, a connection that is worth exploring further.

## 5. Conclusions

In this paper, we determined radial velocities, lithium abundances, and accretion properties of 40 members of the Chamaeleon II star-forming region from FLAMES@VLT optical spectroscopy. Elemental abundances of Fe, Al, Si, Ca, Ti, and Ni for a suitable pre-main sequence star of the region were also measured. Our main results can be summarized as follows:

1. The average radial velocity of the stars is consistent with that of the gas ( $\sim 10 - 12 \text{ km s}^{-1}$ ). The dispersion of the radial velocity distributions of the stars and gas

<sup>5</sup> We considered the IRAC@*Spitzer* fluxes at 3.6, 4.5, 5.8, and  $8.0 \mu\text{m}$  and the MIPS@*Spitzer* fluxes at 24 and  $70 \mu\text{m}$ .

**Table 4.** Spearman’s correlation coefficients ( $\rho$ ) and probabilities ( $p$ ) for different color- $\dot{M}_{\text{acc}}$  relations.

Color	$\rho$	$p$
$Ks-[3.6]$	0.28	24%
$Ks-[4.5]$	0.56	5%
$Ks-[5.8]$	0.52	2%
$Ks-[8.0]$	0.68	1%
$Ks-[24]$	0.29	16%
$Ks-[70]$	0.30	19%
$[3.6]-[4.5]$	0.80	1%
$[3.6]-[5.8]$	0.61	1%
$[3.6]-[8.0]$	0.52	8%
$[5.8]-[8.0]$	-0.07	80%
$[8.0]-[24]$	-0.09	75%
$[24]-[70]$	0.05	85%

- ( $\sim 1 - 2 \text{ km s}^{-1}$ ) are also in agreement. Similar results were found by Dubath et al. (1996) in Chamaeleon I (where  $\langle V_{\text{rad}} \rangle_{\text{Cha I}} \sim 15.0 \pm 0.5 \text{ km s}^{-1}$ ).
2. A binary fraction of 18% is found in Chamaeleon II, which is similar to that in other T associations with comparable star density (see, e.g., the Taurus-Auriga association; Torres et al. 2002).
3. The metallicity of the suitable member is slightly below the solar value, as also found by Santos et al. (2008) for the Chamaeleon Complex.
4. We find an average lithium abundance of the star-forming region of  $2.5 \pm 0.6 \text{ dex}$ .
5. Mass accretion rates derived through several secondary diagnostics (e.g.,  $\text{H}\alpha$ ,  $\text{H}\beta$ ,  $\text{He I } \lambda 5876 \text{ \AA}$ , and  $\text{He I } \lambda 6678 \text{ \AA}$ ) are consistent with each other, justifying the use of all of them to compute an average mass accretion rate for each star.
6. We provide a relationship between accretion luminosity,  $L_{\text{acc}}$ , and the luminosity of the  $\text{He I } \lambda 7065 \text{ \AA}$  line.
7. The relationship between mass accretion rate ( $\dot{M}_{\text{acc}}$ ) and stellar mass ( $M_{\star}$ ) in Chamaeleon II is consistent with that found by previous studies in other T associations.
8. Although slightly lower, the average mass accretion rate in Chamaeleon II fits well the relationship  $\dot{M}_{\text{acc}}$  versus  $\text{Age}$  reported by Sicilia-Aguilar et al. (2010).
9. We cannot exclude that significant variability on timescales longer than the time span of our observations and possibly due to episodes of variable mass accretion may produce the vertical scatter observed in the  $\dot{M}_{\text{acc}}$  versus  $M_{\star}$  plot. However, we suggest that such scatter of about two orders of magnitude in  $\dot{M}_{\text{acc}}$  at a given mass is also affected by other stellar properties.

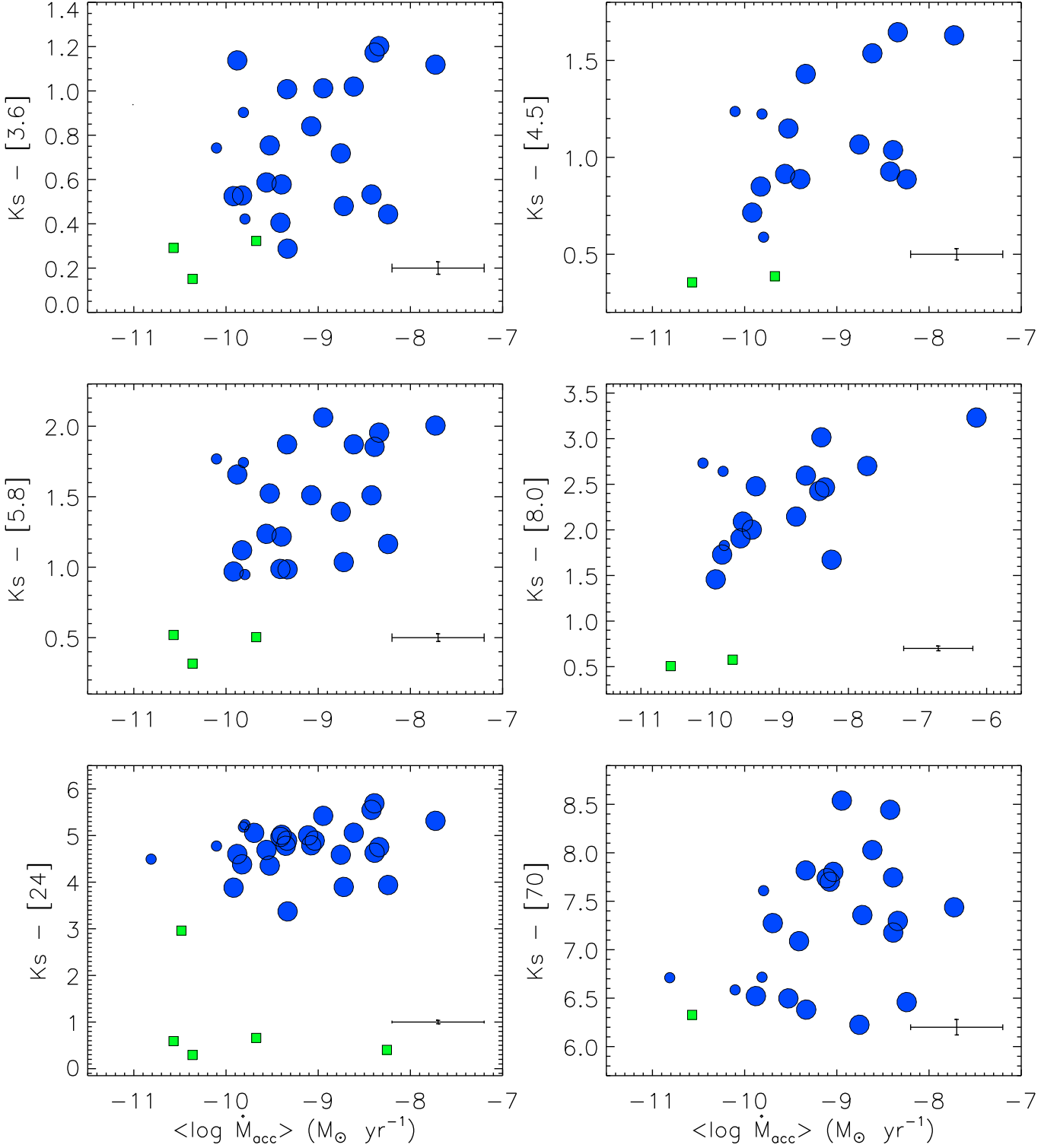


**Fig. 10.** Infrared *2MASS-Spitzer* colors versus mean mass accretion rates. Squares and dots correspond to Class III and Class II objects, respectively (see Table 7). Symbol sizes represent stars with  $EW_{H\alpha} < 10 \text{ \AA}$  (small squares and dots) and with  $EW_{H\alpha} > 10 \text{ \AA}$  (big dots). Mean error bars are overplotted on the lower right corner of each panel.

10. The color- $\dot{M}_{\text{acc}}$  relationships suggest that the circumstellar disks in Cha II become optically thin at  $\sim 10^{-10} M_{\odot} \text{ yr}^{-1}$ .
11. The fraction of accretors in Chamaeleon II is  $\sim 50\%$ , which, according to the evolution of mass accretion rate

in star-forming regions by Fedele et al. (2010), is consistent with the estimated age for the region ( $\sim 3 \text{ Myr}$ ).

*Acknowledgements.* The authors are very grateful to the referee Ralph Neuhauser for carefully reading the paper and for his useful remarks. This research made use of the SIMBAD database, operated

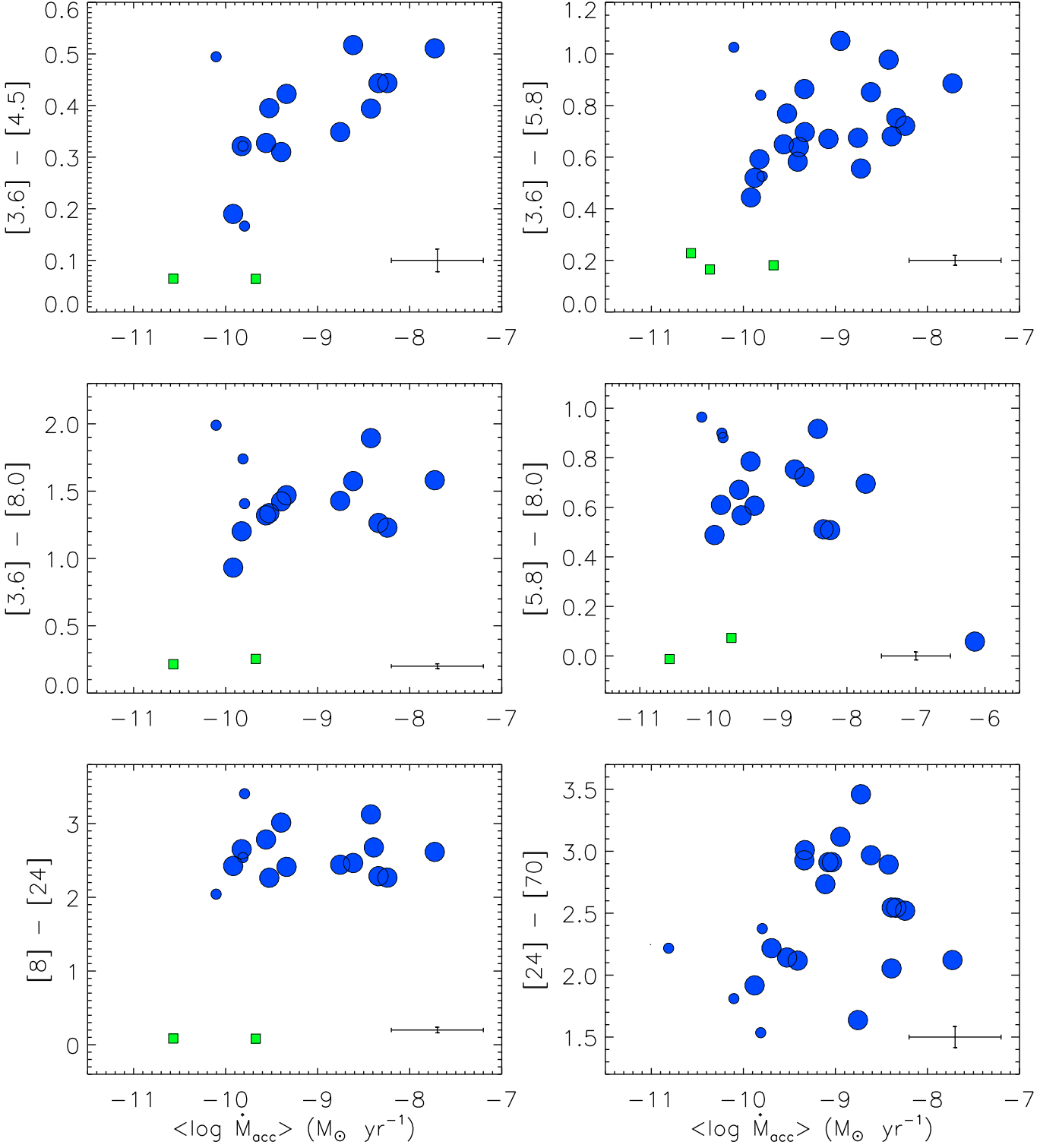


**Fig. 11.** *Spitzer-Spitzer* colors versus mean mass accretion rates. Symbols as in Fig. 10. Mean error bars are overplotted on the lower right corner of each panel.

at the CDS (Strasbourg, France). KB acknowledges the funding support from the INAF Postdoctoral fellowship. We thank S. Antonucci for discussions on accretion luminosity from the Br $\gamma$  line. We thank G. Capasso and F. Cioffi for their support with the OAC computers. We also thank G. Attusino for his warm assistance during the preparation of the manuscript.

## References

- Alcalá, J. M., Spezzi, L., Frasca, A., et al. 2006, *A&A*, 453, 1
- Alcalá, J. M., Spezzi, L., Chapman, N., et al. 2008, *ApJ*, 676, 427
- Alcalá, J. M., Biazzo, K., Covino, E., & Frasca, A. 2011, *A&A*, 531, 12

- Alcalá, J. M., Stelzer, B., Covino, E., et al. 2011b, *Astronomische Nachrichten*, 332, 242
- Allers, K. N., Kessler-Silacci, J. E., Cieza, L. A., & Jaffe, D. T. 2006, *ApJ*, 644, 364
- Antoniucci, S., García-López, R., Nisini, B., et al. 2011, *A&A*, 534, 32
- Biazzo, K., Randich, S., & Palla, F. 2011, *A&A*, 525, 35
- Biazzo, K., Randich, S., Palla, F., & Briceño, C. 2011, *A&A*, 530, 19
- Blecha, A., Cayatte, V., North, P., Royer, F., & Simond, G. 2000, *Proc. SPIE*, 4008, 467
- Cabrit, S., Edwards, S., Strom, S. E., & Strom, K. M. 1990, *ApJ*, 354, 687
- Covino, E., Alcalá, J. M., Allain, S., et al. 1997, 328, 187
- D'Alessio, P., Calvet, N., Hartmann, L., Franco-Hernández, R., & Servín, H. 2006, *ApJ*, 638, 314
- D'Antona, F., & Mazzitelli, I. 1997, *MSAIt*, 68, 807
- D'Orazi, V., & Randich, S. 2009, *A&A*, 501, 553
- D'Orazi, V., Biazzo, K., & Randich, S. 2011, *A&A*, 526, 103
- De Marchi, G., Panagia, N., Romaniello, M., et al. 2011, *ApJ*, 740, 11
- Dubath, P., Reipurth, B., & Mayor, M. 1996, *A&A*, 308, 107
- Ercolano, B., & Clarke, C. J. 2010, *MNRAS*, 402, 2735
- Evans, N. J., II, Allen, L. E., Blake, G. A., et al. 2003, *PASP*, 115, 965
- Fang, M., van Boekel, R., Wang, W., et al. 2009, *A&A*, 504, 461
- Fedele, D., van den Ancker, M. E., Henning, Th., Jayawardhana, R., & Oliveira, J. M. 2010, *A&A*, 510, 72
- García López, R., Nisini, V., Antoniucci, S., et al. 2011, *A&A*, 534, 99
- González-Hernández, J. I., Caballero, J. A., Rebolo, R., et al. 2008, *A&A*, 490, 1135
- Güdel, M., Briggs, K. R., Arzner, K., et al. 2007, *A&A*, 468, 353
- Gullbring, E., Hartmann, L., Briceño, C., & Calvet, N. 1998, *ApJ*, 492, 323
- Hartigan, P., Edwards, S., & Ghandour, L. 1995, *ApJ*, 452, 736
- Hartmann, L. 1998: in *Accretion Processes in Star Formation*, Cambridge Univ. Press
- Hartmann, L., Calvet, N., Gullbring, E., & D'Alessio, P. 1998, *ApJ*, 495, 385
- Hauschildt, P. H., Allard, F., & Baron, E. 1999, *ApJ*, 512, 377
- Herbst, W., Herbst, D. K., Grossman, E. J., & Weinstein, D. 1994, *AJ*, 108, 1906
- Herczeg, G. J., & Hillenbrand, L. A. 2008, *ApJ*, 681, 594
- Johnson, J. A., Aller, K. M., Howard, A. W., & Crepp, J. R. 2010, *PASP*, 122, 905
- Lin, D. N. C., & Papaloizou, J. C. B. 1993: in *Protostars and planets III*, University of Arizona Press, E. H. Levy, & J. I. Lunine eds., p. 749
- Luhman, K. L. 2008: in *Handbook of Star Forming Regions Vol. II*, ASP Conf., B. Reipurth ed., p. 169
- Mizuno, A., Hayakawa, T., Tachihara, K., et al. 1999, *PASJ*, 51, 859
- Modigliani, A., Mulas, G., Porceddu, I., et al. 2004, *The Messenger*, 118, 8
- Muzerolle, J., Hartmann, L., & Calvet, N. 1998a, *AJ*, 116, 455
- Muzerolle, J., Hartmann, L., & Calvet, N. 1998b, *AJ*, 116, 2965
- Natta, A., Testi, L., & Randich, S. 2006, *A&A*, 452, 245
- Palla, F., Randich, S., Pavlenko, Y. V., Flaccomio, E., & Pallavicini, R. 2007, *ApJ*, 659, 41
- Pavlenko, Y. V., & Magazzù, A. 1996, *A&A*, 311, 961
- Porras, A., Jørgensen, J. K., Allen, L. E., et al. 2007, *ApJ*, 656, 493
- Press, W. H., Flannery, B. P., Teukolsky, S. A., & Vetterling, W.T. 1986: in *Numerical Recipes. The Art of Scientific Computing*, Cambridge University Press, p. 489
- Reipurth, B., Pedrosa, A., & Lago, M. T. V. T. 1996, *A&AS*, 120, 229
- Rigliaco, E., Natta, A., Randich, S., Testi, L., & Biazzo, K. 2011a, *A&A*, 525, 47
- Rigliaco, E., Natta, A., Randich, S., et al. 2011b, *A&A*, 526, 6
- Robberto, M., Song, J., Mora Carrillo, G., et al. 2004, *ApJ*, 606, 952
- Santos, N. C., Melo, C., James, D. J., et al. 2008, *A&A*, 480, 889
- Sicilia-Aguilar, A., Henning, T., & Hartmann, L. E. 2010, *ApJ*, 710, 597
- Schisano, E., Covino, E., Alcalá, J. M. et al. 2009, *A&A*, 501, 1013
- Soderblom, D. R., Jones, B. F., & Balachandran, S., et al. 1993, *AJ*, 106, 1059
- Spezzi, L., Alcalá, J. M., Covino, E., et al. 2008, *ApJ*, 680, 1295
- Spezzi, L., De Marchi, G., Panagia, N., Sicilia-Aguilar, A., & Ercolano, B. 2012, *MNRAS*, 421, 78
- Torres, G., Neuhäuser, R., & Guenther, E. W. 2002, *AJ*, 123, 1701
- Tonry, J., & Davis, M. 1979, *ApJ*, 84, 1511
- Yasui, C., Kobayashi, N., Tokunaga, A. T., et al. 2010, *ApJ*, 723, 113
- Young, K. E., Harvey, P. M., Brooke, T. Y., et al. 2005, *ApJ*, 628, 283
- Walker, M. F. 1972, *ApJ*, 175, 89
- White, R. J., Basri, G. 2003, *ApJ*, 582, 1109
- Whittet, D. C. B., Prusti, T., Franco, G. A. P., et al. 1997, *A&A*, 327, 1194

**Table 5.** Observing log, radial velocities, and lithium content.

2MASS Name	Other ID	<i>JD</i> (+2 450 000)	Instr.	# obs.	$V_{\text{rad}}^a$ (km s <sup>-1</sup> )	$EW_{\text{Li}}$ (Å)	$\langle \log n(\text{Li}) \rangle$ (dex)	Comment <sup>b,c</sup>
12531722–7707106	IRAS 12496–7650/DK Cha	3795.7806	GIRAFFE	2	...	0		C/HV; S1, S2
		3797.7351	"		...	0		C/HV; S1, S2
12563364–7645453	Sz 46N	3796.7383	UVES	3	14.9±1.0	0.61	2.4	O1
		3797.8682	"		15.9±0.5	0.54		O1
		3797.8963	"		15.8±2.0	0.52		O1
12565864–7647067	Sz 47	3796.7382	GIRAFFE	3	...	0		C/HV
		3797.8681	"		...	0		C/HV
		3797.8963	"		...	0		C/HV
12571172–7640111	IRAS 12535–7623/CHIIXR 2	3796.7383	UVES	3	10.2±1.3	0.58	2.9	
		3797.8682	"		9.9±1.5	0.58		
		3797.8963	"		9.9±1.8	0.62		
12585614–7630104	WFI J12585611–7630105	3796.7382	GIRAFFE	3	11*	0.53	3.0	
		3797.8681	"		9*	0.54		
		3797.8963	"		11*	0.62		
12590984–7651037	C41	3795.3476	GIRAFFE	1	...	0.24	1.8	BC; S1, S2; N1, N2
12591013–7712139	Iso-Cha II 29	4151.1828	GIRAFFE	2	...	0.57	2.6	BC; S1, S2; N1, N2
		4152.2866	"		...	0.52		BC
13005346–7709086	Sz 48SW/CHIIXR 7	3795.7394	GIRAFFE	3	12*	0.66	2.6	
		3796.8740	"		12*	0.63		
		3797.6925	"		11*	0.63		
13005532–7710222	Sz 50/Iso-Cha II 52/CHIIXR 8	3795.7394	UVES	3	12.5±1.3	0.52	2.4	O1
		3796.8740	"		13.9±1.2	0.54		O1
		3797.6926	"		12.6±1.1	0.52		O1
13005534–7708296	WFI J13005531–7708295	3795.7394	GIRAFFE	1	10*	0.61	2.6	
13005622–7654021	RX J1301.0–7654a	3795.8653	UVES	1	–4.2±2.4	0.59	3.7	SB2
		"	"		32.6±2.7			
13005927–7714027	IRAS F12571–7657/Iso-Cha II 54	3797.6925	GIRAFFE	1	8*	0.30		LSN
13015891–7751218	Sz 51/BC Cha	3795.8943	UVES	2	45.3±0.7	0.42	1.9	SB1; O1, O2; F
		3797.7786	"		14.3±0.7	0.30		O1, O2; F
13021351–7637577	CM Cha/IRAS 12584–7621	3795.8653	GIRAFFE	1	13*	0.43	2.4	
13022287–7734494	C50	3795.8936	GIRAFFE	2	12*	0.57	2.5	
		3797.7785	"		13*	0.41		
13030444–7707027	RX J1303.1–7706	3795.7394	GIRAFFE	3	12.5±0.4	0.61	2.9	
		3796.8740	"		12.2±0.4	0.62		
		3797.6925	"		12.3±0.4	0.62		
13030905–7755596	C51	3795.8936	GIRAFFE	2	12*	0.55	3.1	
		3797.7785	"		11*	0.56		
13042410–7650012	Hn 23	3795.8653	UVES	1	15.2±0.2	0.53	3.2	O1
13042489–7752303	Sz 52	3795.8936	GIRAFFE	2	14*	0.49	1.9	S1, S2; N1, N2
		3797.7785	"		13*	0.48		S1, S2; N1, N2
13045571–7739495	Hn 24	3795.6959	GIRAFFE	3	12±3	0.60	2.9	
		3796.8263	"		11±3	0.61		
		3797.6463	"		11±3	0.61		
		3795.8943	UVES	2	46.6±0.7	0.61	2.9	SB1
		3797.7786	"		14.1±0.8	0.61		
13050855–7733425	Hn 25	3795.6959	GIRAFFE	1	10*	0.47	2.0	
13051269–7730525	Sz 53	3795.6959	GIRAFFE	3	8*	0.40	1.8	S1, S2; N1, N2
		3796.8263	"		10*	0.40		S1, S2; N1, N2
		3797.6464	"		11*	0.43		S1, S2; N1, N2
13052072–7739015	Sz 54/BF Cha	3795.8936	GIRAFFE	2	14*	0.46	3.1	
		3797.7785	"		10*	0.47		
		3795.6960	UVES	3	–1.0±1.4	0.47	3.1	SB2; O1
		"	"		30.9±1.6			
		3796.8263	"		–10.8±2.0	0.47		O1
		"	"		34.0±1.6			
		3797.6464	"		–6.3±2.3	0.47		O1
		"	"		35.4±2.8			
13052169–7738102	SSTc2d J130521.7–773810	4151.2721	GIRAFFE	1	...	0.33		BC; C; S1, S2; N1, N2
13063053–7734001	Sz 55	3795.6959	GIRAFFE	3	8*	0.15	0.6	S1, S2; N1, N2
		3796.8263	"		13*	0.26		S1, S2; N2
		3797.6464	"		13*	0.27		S1, S2; N1, N2
13063882–7730352	Sz 56	3795.6960	UVES <sup>o</sup>	3	...	0.56	2.9	very LSN; O1
		3796.8263	"		...	0.50		very LSN; O1
		3797.6464	"		...	0.53		very LSN; O1
13065656–7723094	Sz 57/C60	3795.6960	GIRAFFE	3	10*	0.54	3.0	
		3796.8263	"		10*	0.57		
		3797.6464	"		10*	0.53		
13065744–7723415	Sz 58/IRAS 13030–7707/C61	3795.6960	GIRAFFE	3	13±4	0.49	3.0	S1, S2
		3796.8263	"		12±5	0.49		S1, S2
		3797.6464	"		12±4	0.48		S1, S2
13070922–7730304	Sz 59/BK Cha	3795.6959	GIRAFFE	3	12±3	0.39	2.3	S2
		3796.8263	"		14±3	0.43		S2
		3797.6464	"		12±2	0.41		S2



Table 5. continued.

2MASS Name	Other ID	<i>JD</i> (+2 450 000)	Instr.	# obs.	$V_{\text{rad}}^a$ (km s <sup>-1</sup> )	$EW_{\text{Li}}$ (Å)	$\langle \log n(\text{Li}) \rangle$ (dex)	Comment <sup>b,c</sup>
13071806–7740529	C62	3795.6959	GIRAFFE	2	13*	0.65	3.0	
		3797.6463	"		8*	0.42		
13072241–7737225	Sz 60W	3795.6960	UVES	3	13.9±0.8	0.49	2.2	
		3796.8263	"		13.2±1.0	0.51		
		3797.6464	"		12.5±0.9	0.53		
13074851–7741214	Hn 26	3795.6959	GIRAFFE	3	11*	0.59	2.3	
		3796.8263	"		10*	0.57		
		3797.6463	"		10*	0.60		
13080628–7755051	Sz 61/BM Cha	3796.6956	GIRAFFE	2	13±3	0.40	2.6	
		3797.8201	"		11±3	0.39		
13082714–7743232	C66	3795.6959	GIRAFFE	4	9*	0.55	2.5	SB1?
		3796.6956	"		8*	0.63		
		3797.6463	"		11*	0.45		
		3797.8201	"		12*	0.30		
13090987–7709437	IRAS F13052–7653NW/CHIIXR 60	4151.2219	GIRAFFE	1	...	0.40	1.9	BC; S2
13091071–7709443	IRAS F13052–7653N/CHIIXR 60	3795.8228	UVES	1	46.7±0.8**	0.61	2.5	SB1?
13095036–7757240	Sz 62	3796.6956	GIRAFFE	2	10*	0.44	1.8	
		3797.8201	"		10*	0.44		
13100415–7710447	Sz 63	3795.8227	GIRAFFE	1	10*	0.54	2.2	
13125238–7739182	2MASS J13125238–7739182	3796.6956	GIRAFFE	2	15*	0.58	3.4	
		3797.8201	"		13*	0.60		
13140369–7753076	Sz 64	3796.6956	GIRAFFE	2	10*	0.43	2.1	
		3797.8201	"		10*	0.43		

Notes:

\* Due to low  $S/N$  ratio, few lines, late spectral type, and/or short wavelength coverage, the radial velocity error may be up to 60%.

\*\* This can be classified as a *bona-fide* PMS star based on other criteria (see Alcalá et al. 2008; Spezzi et al. 2008); its high radial velocity suggests it may be a SB1.

<sup>a</sup> For spectroscopic binaries, the different radial velocity measurements of the corresponding CCF peaks are given.

<sup>b</sup> SB1: single-lined spectroscopic binary; SB2: double-lined spectroscopic binary; SB1?: suspected SB1; BC: bad CCF; C: continuum-type spectrum; HV: heavily veiled star; LSN: low  $S/N$  spectrum.

<sup>c</sup> O1=[O I]  $\lambda$ 6300.8 Å, O2=[O I]  $\lambda$ 6363.8 Å, S1=[S II]  $\lambda$ 6715.8 Å, S2=[S II]  $\lambda$ 6729.8 Å, N1=[N II]  $\lambda$ 6548.4 Å, N2=[N II]  $\lambda$ 6583.4 Å, F=[Fe II] multiplets.

<sup>o</sup> In Spezzi et al. (2008), it was mistakenly reported as GIRAFFE observations.

**Table 6.** Star name (column1); equivalent width, observed flux, and mass accretion rate of the H $\alpha$ , H $\beta$ , He I  $\lambda$ 5876 Å, and  $\lambda$ 6678 Å lines (columns 2–13); He I  $\lambda$ 7065 Å line equivalent width and observed line luminosity (columns 14–15); average  $\dot{M}_{\text{acc}}$  as derived from the H $\alpha$ , H $\beta$ , He I  $\lambda$ 5876 Å, and  $\lambda$ 6678 Å lines (column 16).

ID name	$EW_{\text{H}\alpha}$ (Å)	$\log F^{\text{H}\alpha}$ (erg s $^{-1}$ cm $^2$ )	$\log \dot{M}_{\text{acc}}^{\text{H}\alpha}$ ( $M_{\odot}$ yr $^{-1}$ )	$EW_{\text{H}\beta}$ (Å)	$\log F^{\text{H}\beta}$ (erg s $^{-1}$ cm $^2$ )	$\log \dot{M}_{\text{acc}}^{\text{H}\beta}$ ( $M_{\odot}$ yr $^{-1}$ )	$EW_{\text{He5876}}$ (Å)	$\log F^{\text{He5876}}$ (erg s $^{-1}$ cm $^2$ )	$\log \dot{M}_{\text{acc}}^{\text{He5876}}$ ( $M_{\odot}$ yr $^{-1}$ )	$EW_{\text{He6678}}$ (Å)	$\log F^{\text{He6678}}$ (erg s $^{-1}$ cm $^2$ )	$\log \dot{M}_{\text{acc}}^{\text{He6678}}$ ( $M_{\odot}$ yr $^{-1}$ )	$EW_{\text{He7065}}$ (Å)	$\log L^{\text{He7065}}$ ( $L_{\odot}$ )	$\langle \log \dot{M}_{\text{acc}} \rangle$ ( $M_{\odot}$ yr $^{-1}$ )
IRAS 12496–7650/DK Cha	78.5	9.1	–6.3							0.65	7.0	–6.1			–6.1
	91.5	9.2	–6.2							1.07	7.2	–5.8			
Sz 46N	10.5•	6.7	–9.7	4.6•	6.1	–9.8	0.50	5.2	–9.6	0.06	4.2	–10.5			–9.5
	15.6•	6.8	–9.5	8.5•	6.4	–9.5	0.65	5.3	–9.4	0.07	4.3	–10.4			
	17.4•	6.9	–9.4	5.9•	6.2	–9.7	0.69	5.3	–9.4						
Sz 47	32.5														...
	32.5														
	32.3														
IRAS 12535–7623/CHII XR 2	2.2•	6.0	–9.6	0.8•	5.6	–9.6									–9.8
	1.5•	5.9	–9.8	0.6•	5.5	–9.7									
	1.3•	5.8	–9.8	0.3•	5.2	–10.1									
WFI J12585611–7630105	29.2	6.3	–9.7							0.35	4.2	–10.1			–9.9
	31.2	6.3	–9.7							0.55	4.4	–9.8			
	31.5	6.3	–9.7							0.52	4.4	–9.9			
C41	46.7	6.8	–10.8							0.95	4.9	–10.9	0.18	–7.3	–11.0
Iso-Cha II 29	0.9	5.6	–10.6												–10.6
	1.0	5.7	–10.5												
Sz 48SW/CHII XR 7	9.9•	6.6	–9.9												–9.9
	14.7•	6.8	–9.7												
	8.1•	6.6	–10.0												
Sz 50/Iso-Cha II 52/CHII XR 8	33.8•	6.8	–8.1	9.7•	5.9	–8.6	0.43	4.6	–8.7	0.09	4.1	–9.1			–8.4
	35.4•	6.8	–8.1	11.8•	6.0	–8.5	0.46	4.7	–8.7	0.08	4.0	–9.2			
	30.4•	6.7	–8.1	8.5•	5.9	–8.6	0.32	4.5	–8.9	0.07	4.0	–9.2			
WFI J13005531–7708295	2.1	6.0	–10.4												–10.4
RX J1301.0–7654a	3.1	6.8	–8.6	1.4	6.5	–8.4	0.16	5.6	–7.9						–8.3
IRAS F12571–7657/Iso-Cha II 54	16.0														...
Sz 51	132.5•	8.1	–8.1	39.0•	7.5	–8.3	2.92	6.4	–8.0	1.11	6.0	–8.3			–8.3
	110.0•	8.0	–8.2	26.0•	7.3	–8.5	2.29	6.3	–8.1	0.91	5.9	–8.4			
CM Cha/IRAS 12584–7621	27.6	7.4	–8.6							0.72	5.8	–8.2	0.50	–4.6	–8.4
C50	37.5	6.6	–9.8							1.34	5.1	–9.5	0.39	–6.2	–9.9
	38.3	6.7	–9.8							0.78	4.8	–9.9	0.48	–6.1	
RX J1303.1–7706	2.6	6.1	–9.5												–9.5
	2.7	6.1	–9.5												
	2.6	6.1	–9.5												
C51	9.5	6.0	–9.6												–9.7
	6.3	5.8	–9.8												
Hn 23	11.9	7.4	–8.9	1.5	6.5	–9.5	0.26	5.7	–8.8	0.08	5.2	–9.2			–9.0
Sz 52	49.4	7.1	–9.2							0.70	5.1	–9.4	0.45	–5.6	–9.4
	49.9	7.1	–9.2							0.62	5.1	–9.4	0.43	–5.6	
Hn 24	1.3•	5.8	–10.0												–9.8
	1.2•	5.8	–10.0												
	1.9•	6.0	–9.7												
	1.1	5.7	–10.0	0.9	5.7	–9.6	0.12	4.6	–9.5						
	1.4	5.8	–9.9	0.8	5.6	–9.7									
Hn 25	22.5	6.6	–9.4							0.67	4.9	–9.2	0.54	–5.4	–9.3
Sz 53	145.0•	7.8	–8.2							1.05	5.5	–8.7	1.37	–4.7	–8.6
	46.9•	7.3	–8.8							0.70	5.3	–8.9	0.64	–5.1	
	98.3•	7.6	–8.4							0.91	5.4	–8.8	0.79	–5.0	
Sz 54	23.8	7.7	–7.8												–8.2
	22.7	7.7	–7.8												
	21.2	7.7	–7.9	1.9	6.6	–8.6									
	22.4	7.7	–7.8	2.2	6.7	–8.5									
	22.6	7.7	–7.8	1.2	6.4	–8.8									
SSTc2d J130521.7–773810	26.1									0.21					...
Sz 55	101.1•	7.6	–9.1							2.04	5.7	–9.1	1.39	–5.3	–9.1
	127.2•	7.7	–9.0							1.93	5.7	–9.1	1.41	–5.2	
	130.8•	7.7	–9.0							1.97	5.7	–9.1	1.14	–5.3	

Table 6. continued.

ID name	$EW_{H\alpha}$ (Å)	$\log F^{H\alpha}$ (erg s <sup>-1</sup> cm <sup>2</sup> )	$\log \dot{M}_{acc}^{H\alpha}$ ( $M_{\odot}$ yr <sup>-1</sup> )	$EW_{H\beta}$ (Å)	$\log F^{H\beta}$ (erg s <sup>-1</sup> cm <sup>2</sup> )	$\log \dot{M}_{acc}^{H\beta}$ ( $M_{\odot}$ yr <sup>-1</sup> )	$EW_{He5876}$ (Å)	$\log F^{He5876}$ (erg s <sup>-1</sup> cm <sup>2</sup> )	$\log \dot{M}_{acc}^{He5876}$ ( $M_{\odot}$ yr <sup>-1</sup> )	$EW_{He6678}$ (Å)	$\log F^{He6678}$ (erg s <sup>-1</sup> cm <sup>2</sup> )	$\log \dot{M}_{acc}^{He6678}$ ( $M_{\odot}$ yr <sup>-1</sup> )	$EW_{He7065}$ (Å)	$\log L^{He7065}$ ( $L_{\odot}$ )	$\langle \log \dot{M}_{acc} \rangle$ ( $M_{\odot}$ yr <sup>-1</sup> )
Sz 56	11.1 <sup>•</sup> 14.3 <sup>•</sup> 18.8 <sup>•</sup>	6.1 6.2 6.3	-9.7 -9.5 -9.4	3.5 <sup>•</sup> 12.8 <sup>•</sup> 4.8 <sup>•</sup>	5.1 5.7 5.2	-10.3 -9.7 -10.2	1.90 3.70 2.97	5.0 5.3 5.2	-9.0 -8.6 -8.8	0.60 0.78 0.88	4.7 4.8 4.8	-9.1 -8.9 -8.9			-9.4
Sz 57/C60	23.0 <sup>•</sup> 16.5 <sup>•</sup> 16.2 <sup>•</sup>	6.4 6.3 6.3	-8.7 -8.8 -8.9							0.50 0.39 0.41	4.6 4.5 4.5	-8.5 -8.7 -8.7	0.12 0.11 0.10	-5.9 -5.9 -6.0	-8.7
Sz 58/IRAS 13030-7707/C61	18.2 <sup>•</sup> 14.8 <sup>•</sup> 10.5 <sup>•</sup>	7.6 7.5 7.3	-8.8 -8.9 -9.1								4.6 -10.2 0.08	-8.7 -10.2 -9.4	0.15 0.21 0.20	-5.0 -4.9 -4.9	-8.9
Sz 59	52.8 <sup>•</sup> 35.3 <sup>•</sup> 39.1 <sup>•</sup>	7.7 7.5 7.6	-8.1 -8.3 -8.3							0.44 0.30 0.25	5.6 5.4 5.3	-8.3 -8.5 -8.6	0.48 0.30 0.30	-4.5 -4.7 -4.7	-8.4
C62	37.2 <sup>•</sup> 39.6 <sup>•</sup>	6.6 6.6	-9.7 -9.7							1.40 1.85	5.0 5.2	-9.4 -9.2	0.45 0.60	-6.1 -6.0	-9.6
Sz 60W	25.6 <sup>•</sup> 37.6 <sup>•</sup> 36.8 <sup>•</sup>	7.1 7.2 7.2	-9.3 -9.1 -9.1	7.5 <sup>•</sup> 11.8 <sup>•</sup> 12.4 <sup>•</sup>	6.4 6.5 6.6	-9.6 -9.4 -9.4	1.22 0.93 1.06	5.5 5.4 5.5	-9.1 -9.3 -9.2	0.38 0.31 0.39	5.0 4.9 5.0	-9.5 -9.6 -9.5			-9.3
Hn 26	6.6 <sup>•</sup> 8.1 <sup>•</sup> 13.4 <sup>•</sup>	6.3 6.5 6.7	-10.1 -10.0 -9.7							0.08 0.18 0.11	4.3 4.6 4.4	-10.5 -10.0 -10.2	0.09 0.08 0.11	-6.1 -6.1 -6.0	-10.1
Sz 61/BM Cha	81.1 <sup>•</sup> 64.7 <sup>•</sup>	8.2 8.1	-7.6 -7.8							0.68 0.60	6.1 6.1	-7.7 -7.7	0.80 0.53	-4.0 -4.2	-7.7
C66	20.8 29.1 35.9 25.7	6.5 6.7 6.8 6.6	-10.2 -10.0 -9.9 -10.0							0.67 1.87 2.03 2.10	4.9 5.3 5.4 5.4	-10.0 -9.4 -9.3 -9.3	0.50 0.40 0.99 0.90	-6.2 -6.3 -5.9 -5.9	-9.8
IRAS F13052-7653NW/CHIIXR 60	11.2	6.8	-10.0							0.73	5.4	-9.4	0.50	-5.3	-9.7
IRAS F13052-7653N/CHIIXR 60	2.2	5.9	-10.5	0.5	5.0	-11.0									-10.8
Sz 62	115.8 150.8	7.3 7.4	-8.4 -8.4							0.74 0.98	4.9 5.0	-9.1 -9.0	0.35 0.88	-5.6 -5.2	-8.4
Sz 63	93.6	7.2	-8.9							0.41	4.6	-9.8	0.35	-5.8	-9.4
2MASS J13125238-7739182	5.8 7.0	5.8 5.9	-10.3 -10.2							0.11 0.11	3.9 3.9	-10.5 -10.5			-10.5
Sz 64	132.1 121.4	7.1 7.0	-9.1 -9.1							2.82 3.00	5.3 5.3	-9.0 -9.0	0.79 1.22	-5.9 -5.7	-9.1

Notes:

— • Variable line profile.

**Table 7.** Parameters taken from the literature.

	Sp.T. <sup>a</sup>	$T_{\text{eff}}^{\text{a}}$ (K)	$\langle M_{\star} \rangle^{\text{a}}$ ( $M_{\odot}$ )	$\log L_{\star}^{\text{a}}$ ( $L_{\odot}$ )	$R_{\star}^{\text{a}}$ ( $R_{\odot}$ )	$\langle \log g \rangle^{\text{a}}$ (dex)	$R_{\text{in}}^{\text{a}}$ (AU)	$\langle \text{Age} \rangle^{\text{a}}$ (Myr)	Class <sup>b</sup>
IRAS 12496–7650/DK Cha	F0	7200	2.00	1.27	2.77	3.9	1.79	4.75	II
Sz 46N	M1	3705	0.53	−0.48	1.39	3.9	0.13	3.07	II
Sz 47	...	...	...	...	...	...	0.2*	...	III
IRAS 12535–7623/CHII XR 2	M0	3850	0.67	0.14	2.71	3.4	0.49	0.80	II
WFI J12585611–7630105	M5	3025	0.12	−1.03	1.13	3.4	...	1.33	III
C41	M5.5	3057	0.10	−1.95	0.37	4.3	0.98	13.37	Flat
Iso-Cha II 29	M0	3850	0.65	−0.19	1.85	3.7	70.86	2.77	III
Sz 48SW/CHII XR 7	M1	3705	0.57	−0.58	1.25	4.0	2.06	4.70	II
Sz 50/Iso-Cha II 52/CHII XR 8	M3	3415	0.35	0.06	3.10	3.0	0.07	0.37	II
WFI J13005531–7708295	M2.5	3687	0.53	−0.45	1.46	3.8	0.2*	2.83	III
RX J1301.0–7654a	K5	4350	0.70	0.38	2.67	3.4	0.2*	0.60	III
IRAS F12571–7657/Iso-Cha II 54	...	...	...	...	...	...	0.09	...	II
Sz 51	K8.5	3955	0.73	−0.36	1.37	4.0	0.20	4.67	II
CM Cha/IRAS 12584–7621	K7	4060	0.85	−0.14	1.78	3.9	0.78	3.67	II
C50	M5	3125	0.16	−1.19	0.89	3.8	0.08	2.73	II
RX J1303.1–7706	M0	3850	0.73	0.10	2.61	3.5	0.2*	1.07	III
C51	M4.5	3197	0.19	−0.53	1.77	3.2	0.2*	0.63	III
Hn 23	K5	4350	1.00	−0.06	1.60	4.0	0.18	3.57	II
Sz 52	M2.5	3487	0.35	−0.75	1.15	3.8	0.35	2.83	II
Hn 24	M0	3850	0.65	0.02	2.37	3.5	0.06	1.03	II
Hn 25	M2.5	3487	0.37	−0.48	1.56	3.6	0.19	1.60	II
Sz 53	M1	3705	0.55	−0.49	1.39	3.9	0.03	3.23	II
Sz 54	K5	4350	0.97	0.29	2.42	3.6	0.09	1.37	II
SSTc2d J130521.7–773810	...	...	...	...	...	...	0.65	...	Flat
Sz 55	M2	3560	0.42	−0.90	0.91	4.1	0.08	7.50	II
Sz 56	M4	3270	0.23	−0.47	1.78	3.3	0.43	0.80	II
Sz 57/C60	M5	3125	0.15	−0.39	2.21	2.9	0.05	0.60	II
Sz 58/IRAS 13030–7707/C61	K5	4350	0.97	−0.16	1.43	4.1	1.75	6.93	II
Sz 59	K7	4060	0.82	−0.05	1.96	3.8	0.37	2.20	II
C62	M4.5	3197	0.18	−1.05	0.97	3.7	0.02	1.83	II
Sz 60W	M1	3705	0.57	−0.54	1.32	4.0	0.07	3.57	III <sup>‡</sup>
Hn 26	M2	3560	0.44	−0.59	1.30	3.8	0.23	3.00	II
Sz 61/BM Cha	K5	4350	1.00	0.07	1.87	3.8	0.66	2.67	II
C66	M4.5	3197	0.17	−1.30	0.73	3.9	0.01	6.50	II
IRAS F13052–7653NW/CHII XR 60	M0.5	3777	0.62	−0.70	1.03	4.2	0.11	7.77	II
IRAS F13052–7653N/CHII XR 60	M1.5	3632	0.47	−0.47	1.49	3.8	3.54	2.70	II
Sz 62	M2.5	3487	0.37	−0.48	1.56	3.6	0.05	1.60	II
Sz 63	M3	3415	0.32	−0.64	1.38	3.7	3.02	1.50	II
2MASS J13125238–7739182	M4.5	3197	0.19	−0.81	1.28	3.5	0.03	1.43	III
Sz 64	M5	3125	0.16	−1.04	1.04	3.6	0.18	1.67	II

Notes:

<sup>a</sup> Spectral types, effective temperatures, luminosities, and radii are from Spezzi et al. (2008). Masses and ages are the average of three values reported in Spezzi et al. (2008) and derived using three different sets of evolutionary models, with mean standard deviations of  $\sim 0.15M_{\odot}$  and  $\sim 1.8$  Myr, respectively. Mean surface gravities were computed through the relation:  $\langle \log g \rangle = 4.4377 + \langle \log M_{\star} \rangle + 4 \log T_{\text{eff}}/5777 - \log L_{\star}$ .  $R_{\text{in}}$  was adopted from Alcalá et al. (2008).

<sup>b</sup> Lada Class as derived in Alcalá et al. (2008).

<sup>‡</sup> In Alcalá et al. (2008), it appears as Class III, but it is a Class II object.

\*  $R_{\text{in}} = 5R_{\star}$  (see Section 3.4).

**To be published in electronic form only**

## Appendix A: Examples of H $\alpha$ /H $\beta$ line profiles

Here, we display the H $\alpha$  (Figs. A.1, A.2) and H $\beta$  (Figs. A.3) profiles of the targets showing changes in their line shape and/or intensity. Below, we briefly comment on each object.

*Sz 48SW.* During the first observing night, the spectrum showed a symmetric, relatively narrow H $\alpha$  emission profile with a peak close to the line center (type I profile, following the classification of Reipurth et al. 1996). During the second night, the profile appeared slightly asymmetric with lower emission on the blue than on the red side (type IIIB), and then turned back to the type I profile on the third night.

*Hn 24.* The H $\alpha$  line profile changes from type IVR (an inverse P-Cygni-like profile) during the first two nights to type IIIR, where less emission in the red than in the blue is seen.

*Sz 53.* The H $\alpha$  line shows always a type IIB profile, with a central reversal at the line center and the blue-wing peak intensity lower than the red one. The line strength changes, being maximum during the first observation. The secondary peak always exceeds half the strength of the primary peak. This type of peak is probably due to the interplay of variable accretion and mass loss.

*Sz 55.* This star shows an H $\alpha$  line profile changing from IIB to IIIB (where the secondary peak is slightly less intense than half the strength of the primary peak) to IIB.

*Sz 57.* It always shows a narrow and symmetric H $\alpha$  emission type I profile with a peak close to the line center.

*Sz 58.* The H $\alpha$  profile changes from IIIR (first night) to IIR (second and third night).

*Sz 59.* IIR/IIR/IIIR profiles are observed for this star during the three observations.

*Hn 26.* This star shows IIR/IIB/IIB H $\alpha$  line profiles.

*Sz 61.* It shows an H $\alpha$  profile slightly changing from IIB type to IIIB.

*Sz 46N.* This star shows H $\alpha$  and H $\beta$  line profiles that are always symmetric (type I).

*IRAS 12535-7623.* The H $\alpha$  and H $\beta$  emission line profiles are always consistent with type I.

*Sz 50.* Its H $\alpha$  and H $\beta$  emission line profiles are always narrow and almost symmetric (type I).

*Sz 51.* H $\alpha$  and H $\beta$  are always of type I.

*Sz 56.* The H $\alpha$  profile changes from IIR (during the first and second night) to IIIR (third night), while the H $\beta$  profile is always of type I.

*Sz 60W.* The H $\alpha$  line has a complex profile, starting from IIB type during the first night; during the second night, it shows broad wings, red-shifted and blue-shifted absorption, and a narrow emission in the center (like a YY Orion H $\alpha$  profile, normally associated with high infall and outflow rates, consistent with the high value of  $\dot{M}_{acc}$ ; Walker 1972); during the third night, it turned back to a IIB type profile. The H $\beta$  line changes from YY Orionis H $\beta$ -like profile to type IIIR to type I.

## Appendix B: Stellar variability



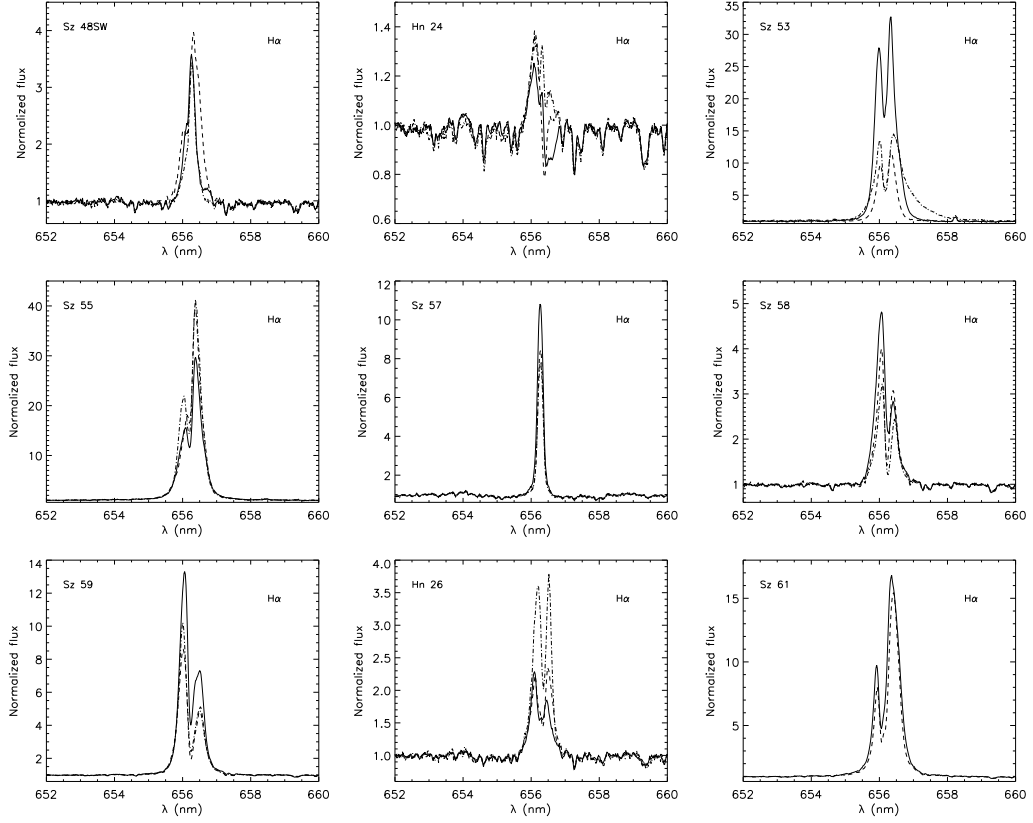


**Fig. A.1.** Examples of  $H\alpha$  emission line profile variations of nine stars. The fluxes are normalized to the continuum. The data refer to the FLAMES/GIRAFFE configuration. The solid/dashed/dash-dotted line represents the first/second/third observation, respectively.

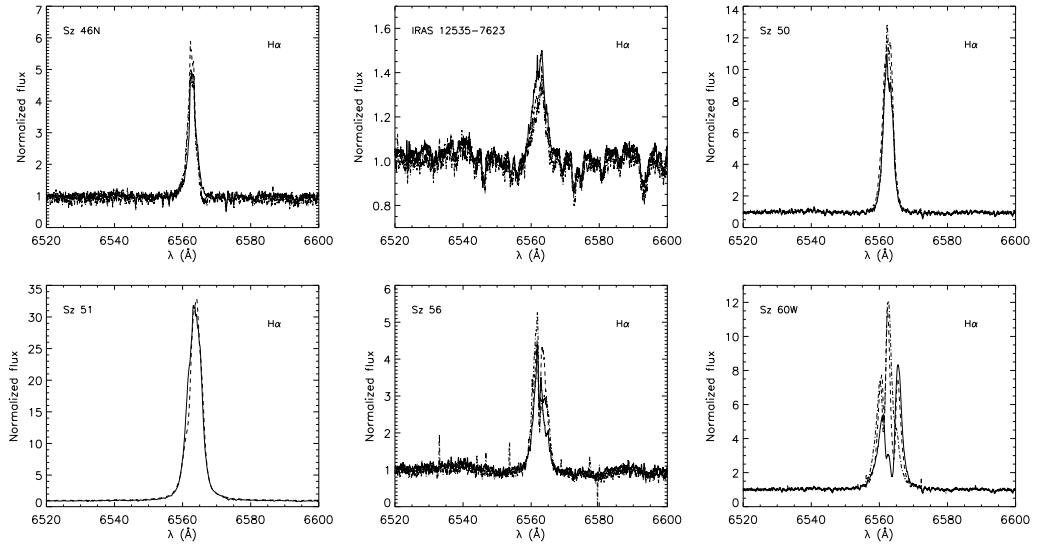


**Fig. A.2.** Same as in Fig. A.1, but for the UVES data.

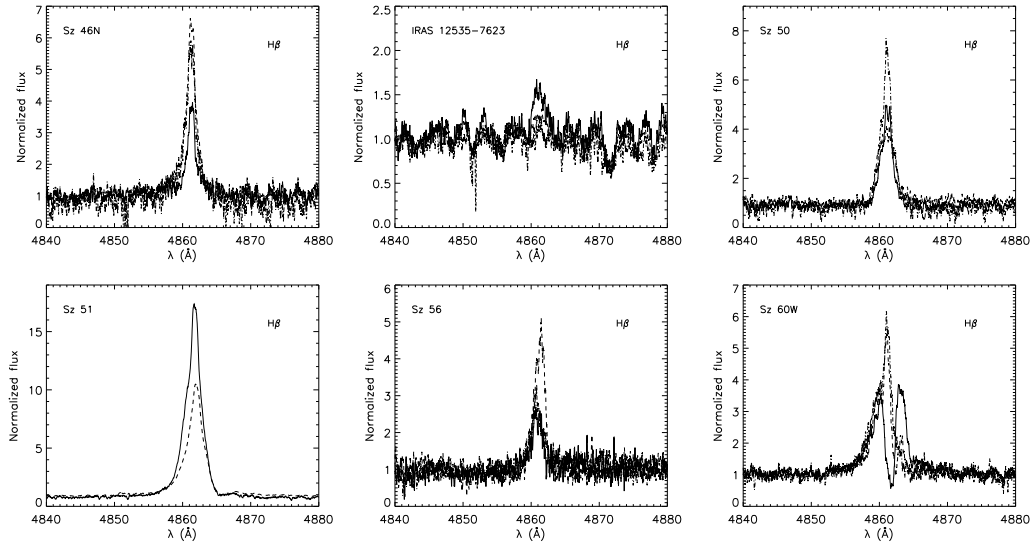


**Fig. A.3.** Same as in Fig. A.1, but for the UVES data and the H $\beta$  profiles.

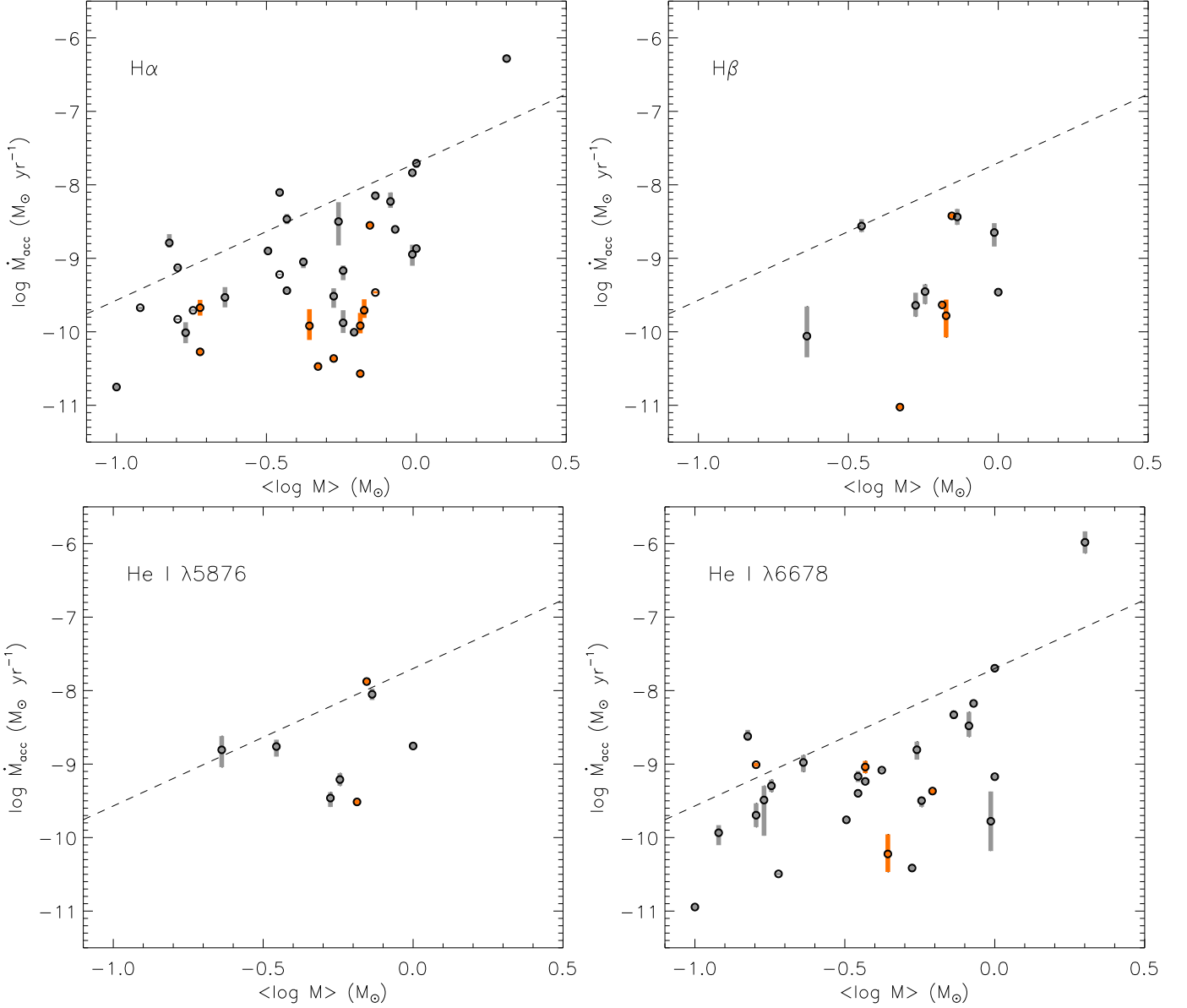


**Fig. B.1.** Mass accretion rates measured from the H $\alpha$  (left top panel), H $\beta$  (right top panel), He I  $\lambda 5876$  Å (left bottom panel), and He I  $\lambda 6678$  Å (right bottom panel) lines versus mass. Vertical bars connect the minimum and maximum values of  $\dot{M}_{\text{acc}}$  obtained per each star at different epochs. Stars are divided into high H $\alpha$  emitters ( $EW_{\text{H}\alpha} > 10$  Å; grey bars) and low H $\alpha$  emitters ( $EW_{\text{H}\alpha} < 10$  Å; orange bars), i.e., stars where the line emission cannot be unambiguously attributed to accretion activity, as it is most likely caused by chromospheric activity. The dashed line shows the relation  $\dot{M}_{\text{acc}} \propto M_{\star}^{1.87}$  obtained by Herczeg & Hillenbrand (2008) for Taurus members. The highest  $\dot{M}_{\text{acc}}$  values in the first and fourth panels refer to the early-type star DK Cha. The lower number of points in the H $\beta$  and He I plots is due to two reasons: absence of the line in the given star or line out of the wavelength range (see Table 5).